Paraglacial adjustment of alluvial fans to the last deglaciation in the Snežnik Mountain, Dinaric karst (Slovenia)

Žebre, Manja; Jež, Jernej; Mechernich, Silke; Muši, Branko; Horn, Barbara; Jamšek Rupnik, Petra

Published in:
Geomorphology

DOI:
10.1016/j.geomorph.2019.02.007

Publication date:
2019

Citation for published version (APA):
Žebre, M., Jež, J., Mechernich, S., Muši, B., Horn, B., & Jamšek Rupnik, P. (2019). Paraglacial adjustment of alluvial fans to the last deglaciation in the Snežnik Mountain, Dinaric karst (Slovenia). *Geomorphology*, *332*, 66-79. https://doi.org/10.1016/j.geomorph.2019.02.007

Paraglacial adjustment of alluvial fans to the last deglaciation in the Snežnik Mountain, Dinaric karst (Slovenia)

Manja Žebre[a *], Jernej Jež[a], Silke Mechernich[b], Branko Mušič[c, d], Barbara Horn[c], Petra Jamšek Rupnik[a]

[a] Geological Survey of Slovenia, Dimičeva ulica 14, 1000 Ljubljana, Slovenia
[b] Institute for Geology and Mineralogy, University of Cologne, Zuelpicherstr. 49b, 50937 Köln, Germany
[c] GEARH d.o.o., Radvanjska 13, 2000 Maribor, Slovenia
[d] University of Ljubljana, Department of Archaeology, Aškerčeva 2, 1000 Ljubljana, Slovenia

Corresponding author. E-mail address: manjazebre@gmail.com, maz24@aber.ac.uk (M. Žebre).

Present address: Department of Geography & Earth Sciences, Aberystwyth University, Llandinam Building, Penglais Campus, SY23 3DB, Aberystwyth, United Kingdom

Abstract

Glaciokarst depressions are major glacigenic depocenters in the Dinaric mountain karst areas and often store important information about the timing and nature of glacial processes and paraglacial sediment reworking. This study focuses on Praprotna draga, which is one of the largest glaciokarst depressions in the Snežnik Mountain (Dinaric karst), with an area of ~3.4 km^2 and a maximum depth of 140 m. The western slopes of the depression are characterized by undulated moraine morphology and alluvial fans are filling its entire floor. We present the results on the thickness, origin and age of the sediment infill using a complementary geomorphological, sedimentological, geophysical and dating approach. Distribution of moraines point to two glacial advances that were associated with two main alluvial fan aggradation phases recognised using the electrical resistivity tomography measurements. The youngest alluvial deposits were sampled for cosmogenic ^{36}Cl analysis using amalgamated carbonate pebbles. The depth profile of ^{36}Cl concentrations suggests an age of 12.3 ± 1.7 ka when assuming a likely denudation rate of 20 mm ka^{-1}. Since the existence of the Younger Dryas glaciers in the study area is climatically difficult to explain, we tentatively propose that the youngest alluvial deposition in Praprotna draga took place after the glacier retreat during the paraglacial period. Our findings suggest that the time window of paraglacial adjustment in the Snežnik Mountain was brief and likely conditioned by quick recolonization with vegetation and inefficient surface runoff on deglaciated karst terrain.

Keywords: Dinaric karst, Electrical Resistivity Tomography, Cosmogenic dating, Younger Dryas, Paraglacial

1. Introduction

Little information is currently available about the deglaciation of Dinaric karst and the Balkan Peninsula, and even less is known on the nature of paraglacial sedimentation in this same area. Although Dinaric karst is known for widespread and well-developed karst phenomena (Cvijić, 1893) and is referred to as *locus typicus* for the karst worldwide, it is also of interest because its mountainous parts experienced glaciations during the Quaternary cold stage climates, resulting in a glaciokarst type of landscape (Smart, 2004; Žebre and Stepišnik, 2015). The last deglaciation of the Dinaric mountain karst areas is chronologically still poorly constrained. For example, the Younger Dryas deglaciation has been dated in the Orjen Mountain (Montenegro) (Hughes et al., 2010), Šar Planina (Kuhlemann et al., 2009) and Galičica mountains (Ribolini et al., 2011; Gromig et al., 2018) (both located in FYROM), and Mount Chelmos (Pope et al., 2015) and Mount Olympus (Styllas et al., 2018) (both located in Greece), whereas the Oldest Dryas deglaciation has been recorded in the Mount Pelister (FYROM) (Ribolini et al., 2018). However, data on the last deglaciation elsewhere in the Balkans are generally missing (e.g., Milivojević et al., 2008; Žebre and Stepišnik, 2014).

On the other hand, the glacial geomorphology in Dinaric karst is relatively well-studied (e.g., Milivojević et al., 2008; Žebre and Stepišnik, 2014; Krklec et al., 2015). Closed depressions, which are characteristic features for Dinaric karst (Mihevc and Prelovšek, 2010), are also present in other karst landscapes that were once glaciated, such as the Julian Alps (Colucci, 2016) and Dachstein Mountains (Veress, 2017) in the European Alps, Picos de Europa (Smart, 1986) and Taurus Mountains (Sarıkaya and Çiner, 2017). These so-called “glaciokarst depressions” (Ćalić, 2011; Veress, 2017), particularly those located at the edge of terminating glaciers and thus experiencing key aggradation phases, are major depocenters for glacigenic deposits in karst areas (Adamson et al., 2014; Žebre et al., 2016). As a result, glaciokarst depressions often host valuable proxy-data, which are important sources of information for palaeoenvironmental and palaeolandscape studies.

Glaciers produce vast amounts of sediments that are later transported, deposited and reworked by fluvial streams, but it is not always clear whether these sediments were deposited directly by meltwaters, or rather at the end of, or after glacier retreat. Fluvial aggradation in glacial catchments primarily takes place during phases of glacial advance, when glaciers are eroding and exporting sediment downstream, and also for the period of paraglacial adjustment, when glacially conditioned sediments are being reworked (Cordier et al., 2017). Paraglacial processes tend to adjust the relief to non-glacial conditions, thus generating a transitional landscape (Slaymaker, 2009), which starts at deglaciation and terminates when sediment yields drop to rates which are typical of unglaciated catchments (Ballantyne, 2002; Mercier, 2008). The duration and intensity of paraglacial adjustment depends on the amount of sediment deposited at palaeo-glacier margins, the rate of slope erosion processes and environmental conditions such as post-glacial climate, timing of vegetation change, catchment size and morphology (Church and Slaymaker, 1989; Harbor and Warburton, 1993; Ballantyne, 2003; Cordier et al., 2017). Although it has been suggested that the paraglacial period in the karst areas of the Balkan Peninsula was short-lived due to quick recolonization with vegetation and subsequent stabilization of deglaciated terrain (Adamson et al., 2014; Woodward et al., 2014), there are still several uncertainties about the timing of paraglacial adjustment and the nature of sediment reworking in this area. These are the key for understanding the evolution of deglaciated glaciokarst landscapes. Therefore, this paper aims at unravelling and better constraining the timing of paraglacial sedimentation in the Snežnik Mountain (Dinaric karst, Slovenia) (Fig. 1) by studying the sediment infill of the Praprotna draga karst depression using geomorphological mapping, sediment facies analysis, electrical resistivity tomography measurements and cosmogenic ^{36}Cl nuclide exposure dating. The interpretation of the results from Praprotna draga is supported by the geomorphological map of the entire Snežnik area (Žebre and Stepišnik, 2016).

2. Regional setting

Snežnik Mountain is located in the southern part of Slovenia, close to the national border with Croatia and represents a NW continuation of the Gorski Kotar mountainous area (Fig. 1a). The highest altitude in this area is Veliki Snežnik peak (1796 m a.s.l.).

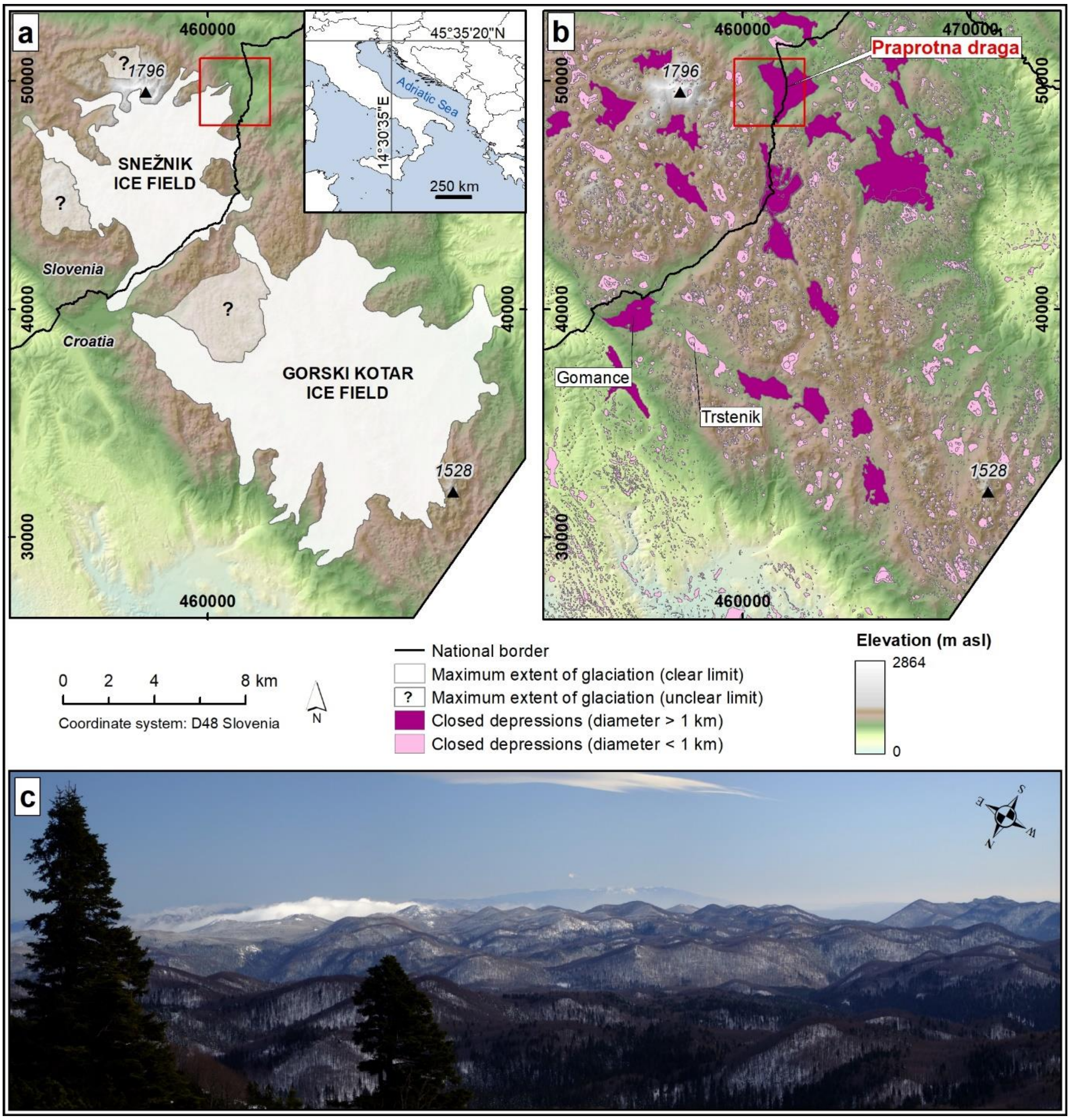

Fig. 1: (a) The maximum recorded phase of glaciation in the Snežnik and NW Gorski kotar area (modified after Žebre and Stepišnik (2016)). (b) Distribution of closed depressions in the Snežnik and NW Gorski Kotar, extracted from a 10 m DEM using the algorithm designed by Grlj and Grigillo (2014). The Praprotna draga study area in (a) and (b) is marked with a red square. (c) Photo of the Snežnik area southeast of the highest peak, where the high grade of karstification is visible in the widespread dolines (photo courtesy of Renato R. Colucci).

2.1. Geology, geomorphology and former chronological data

The Snežnik area belongs to the northwestern part of the External Dinarides, a SW-verging fold-and-trust belt (e.g., Placer, 1998; Vrabec and Fodor, 2006). Due to intense tectonic shortening during the Cenozoic, the area is divided into several thrusts (Placer, 1998). Snežnik and Gorski Kotar represent a part of the Snežnik thrust, a vast tectonic unit that covers a large part of SW Slovenia, predominantly composed of Mesozoic carbonates. The Veliki Snežnik area is mainly composed of bedded to thin bedded Upper Jurassic to Lower Cretaceous limestone, while locally bedded dolomite and limestone-dolomite breccia are also common. Fold and thrust structure is dissected by NW-SE-striking dextral faults and associated NNW-SSE-striking faults belonging to the Dinaric Fault System and representing the neotectonic structural style visible in mountain morphology (e.g., Vrabec and Fodor, 2006; Moulin et al., 2016). Limestone in the Snežnik area is subjected to a rapid karstification resulting in many karstic features (e.g., vertical shafts, sinkholes).

Quaternary sediments have been documented already during geological investigations in the late 1950s and 1970s (Šifrer, 1959; Šikić et al., 1972). These sedimentary bodies of glacigenic origin stand out from the surrounding karstic areas (Figs. 1b and 1c), especially due to their characteristic morphological features. No rock glacier remnants or macro periglacial features exist in the area according to past studies (Colucci et al., 2016; Oliva et al., 2018). The majority of glacial deposits in the form of up to ~50 m high lateral and frontal moraines are distributed on the southern and eastern slopes at elevations between 900 and 1200 m a.s.l. They reach the lowest altitudes in the Gomance karst depression on the southern slopes of Snežnik (900 m a.s.l., Fig. 1b). The western part of Snežnik is dominated by hummocky moraines, reaching down to 1060 m a.s.l. Moraines on the northeastern side are mainly located around the Praprotna draga karst depression, while surprisingly no glacial evidence was identified north of the highest peak (Žebre and Stepišnik, 2016). Typical glacial erosional forms are not common for the Snežnik area. Small glacial erosional features such as striae and chattermarks are almost entirely absent, which is likely a result of high dissolution rates. Other characteristic erosional forms for mountain glaciation, such as cirques and U-shaped valleys, are rare as well (Žebre and Stepišnik, 2016). On the other hand, the area is dissected by glaciokarst depressions, which are most likely formed primarily by karst processes and subglacial erosion (e.g., Smart, 1986; Žebre and Stepišnik, 2015).

The largest and the deepest depressions here reach more than 2 km in diameter and 140 m in depth, having floors filled with glacigenic deposits. In the Gomance karst depression (Fig. 1b) on the southern flanks of the Snežnik massif, a bone found in outwash deposits was dated to 18.7 ±1.0 cal ka BP (recalculated with IntCal13 calibration; Reimer et al., 2013) (Marjanac et al., 2001). This age points to an outwash event during the largest recognized extent of the Snežnik and the nearby Gorski Kotar ice fields, which is estimated to at least 140 km^2 during the Last Glacial Maximum (LGM) (Žebre et al., 2016) (Fig. 1a). In the Trstenik karst depression (950 m a.s.l.) (Fig. 1b), located less than 2 km east of Gomance, pollen analyses indicate the presence of Late-glacial lacustrine deposits at a depth of ~2 m (Šercelj, 1971). In contrast to Gomance, where the floor is predominantly filled with outwash and till deposits, Trstenik mainly hosts peat and gyttja underlain by proglacial lacustrine deposits.

2.2. Climate and vegetation

Due to the proximity of Snežnik to the cyclogenetic area of the northern Adriatic Sea and the Genova Bay, the present climate in the study area is characterized by high precipitation (Isotta et al., 2014), intensified by the orographic effect (Zaninović et al., 2008). Mean annual precipitation (MAP) for the period 1931–1960 at Gomance (937 m a.s.l.) was 2792 mm and mean annual air temperature was 6.6 °C (Pučnik, 1980), but the highest elevations currently receive a MAP of >3500 mm and the mean annual air temperature there was estimated to 2–3 °C (Zaninović et al., 2008). The mean seasonal snow cover duration for the period 1961/62-1990/1991 is 100–150 days and mean seasonal fresh snow accumulation for the same period is 280–420 cm (http://meteo.arso.gov.si/met/en/climate/maps/).

The dominant vegetation community in the Snežnik high karst plateau consists of Dinaric silver fir—European beech forest (*Omphalodo-Fagetum*), with European beech (*Fagus sylvatica*), silver fir (*Abies alba*), and Norway spruce (*Picea abies*) as the dominant tree species (Surina and Wraber, 2005; Kobal et al., 2015). Spruce forest occurs only azonally and is generally confined to dolines as a result of temperature inversion. The tree line is situated at ~1500 m a.s.l. and is marked by presence of subalpine beech stands (*Polysticho lonchitis-Fagetum*) (Surina and Wraber, 2005; Komac et al., 2012).

3. Methods

In this paper, we combine various methods including high-resolution geomorphological mapping, sediment facies analyses, cosmogenic nuclide dating and geophysical measurements to study the sedimentological composition, geometry and age of deposits filling the Praprotna draga karst depression in the Snežnik Mountain.

3.1. Geomorphological mapping

The glacial geomorphological map of Praprotna draga (Fig. 2a) was obtained by updating the previously published geomorphological map of glaciokarst features in Snežnik and NW Gorski Kotar area by Žebre and Stepišnik (2016). We mapped the geomorphological features in the Praprotna draga karst depression by means of field mapping, supported by 1:10.000 and 1:25.000 topographic maps and 1-m resolution digital elevation model (DEM), derived from LiDAR data (Ministry of the Environment and Spatial Planning, Slovenian Environment Agency) with relative horizontal and vertical accuracies of 0.30 and 0.15 m, respectively. With the analysis of LiDAR data we updated the previously published geomorphological map, which was based on topographic maps. The LiDAR data is most suitable for geomorphological mapping due to dense forest cover and in parts dense undergrowth. A LiDAR DEM was processed to produce several maps (shaded relief, topographic curves with 1 m equidistance, slope degree map, slope aspect map) that served as a basis for detailed mapping of individual alluvial fans and moraines.

3.2. Sedimentological characterization

In the area of the mapped alluvial fans and moraine ridges we logged in detail seven up to 2.7 m deep outcrops (3 road cuttings and 4 trenches) (Figs. 3 and 4). We identified key sediment parameters such as sedimentary structures, colour, clast lithology, size, distribution and roundness by using standard field techniques. Lithofacies codes from Evans and Benn (2004) were used for sediment description, which was based on macroscopic observations. We used these data as ancillary information for the geomorphological interpretation of sediment depositional environment and establishing a relationship between electrical resistivity tomography (ERT) data and sedimentary bodies.

3.3. Cosmogenic ^{36}Cl nuclide exposure dating

Given the lack of suitable dating material for radiocarbon (absence of organic material within the deposits) and luminescence (lack of quartz and feldspar) methods, we estimated the age of alluvial fans using cosmogenic exposure dating. This dating method is based on the formation of radionuclides due to the interaction of cosmic rays that occur at a calculatable rate. While in quartz-bearing lithologies cosmogenic radionuclide ^{10}Be is nowadays used almost routinely to constrain ages of late Quaternary landforms (Dunai, 2010; Schmidt et al., 2011; Ruszkiczay-Rüdiger et al., 2016b; Ribolini et al., 2018), the cosmogenic nuclide ^{36}Cl is the nuclide of choice for carbonate lithologies (Frankel et al., 2007; Gromig et al., 2018; Marrero et al., 2018; Mechernich et al., 2018; Styllas et al., 2018). When dating depositional surfaces such as debris flows or alluvial fans, it is necessary to take into account that cosmogenic nuclides are not only produced after formation of the respective surfaces, but also during erosion of the host rock and sedimentary transport of clasts. We obtained this pre-depositional nuclide component (i.e. inherited component) by using a depth profile (e.g., Hancock et al., 1999; Braucher et al., 2011; Schmidt et al., 2011; Rixhon et al., 2018).

3.3.1. Sampling strategy

We sampled one alluvial fan profile (PD-02; Figs. 2 and 3, Table 1) for cosmogenic ^{36}Cl depth profile analysis. Since the available limestone clasts are rather small (diameter of ~3–9 cm), the amount of material from individual clasts is too low for a precise measurement. Hence, limestone clasts within depth intervals of 5 cm were amalgamated to samples composed of 5–6 clasts (Table 2). All selected clasts were subangular to subrounded limestones, with a similar diameter of 3–9 cm. The amount of comparable clasts in a horizontal distance of ±1 m was scarce, hence no further clasts were used for an amalgamation. Since bioturbation and denudation processes likely changed the concentration of cosmogenic nuclides at the surface (Hein et al., 2009), we took only subsurface samples.

Outcrop ID	Elevation (m a.s.l)	Latitude (N)	Longitude (E)
ME-01	1230	45°35'20.81"	14°29'0.68"
ME-02	1013	45°35'15.82"	14°29'43.87"
ME-03	995	45°35'30.66"	14°29'30.47"
PD-01	852	45°35'40.64"	14°29'34.73"
PD-02	837	45°35'48.29"	14°29'55.71"
PD-03	797	45°35'26.34"	14°30'0.47"
PD-06	782	45°35'25.67"	14°30'51.30"

Table 1. Elevations and coordinates of the studied outcrops.

Sample name	Depth interval (cm)	Amount of pebbles	Size of pebbles (cm)	Dissolved amount of sample (g)	Cl spike (*mg*)	Ca conc. ICP-OES (%)	Blank correction (%)	Stable Cl (µg/g)	^{36}Cl (10^5 atoms/g)	± ^{36}Cl (%)
CRN PD-02/ 25-30	25-30	5	5-8	20.1379	1.4848	37.7%	0.41%	47.3 ± 1.9	5.11 ± 0.23	4.4%
CRN PD-02/ 75-80	75-80	5	3-6	20.4658	1.4892	38.3%	0.66%	48.5 ± 2.0	3.14 ± 0.16	5.0%
CRN PD-02/ 105-110	105-110	6	4-9	19.7269	1.4859	38.7%	0.82%	49.7 ± 2.0	2.61 ± 0.11	4.4%
CRN PD-02/ 215-220	215-220	5	3-6	29.6144	1.4832	37.3%	0.48%	49.6 ± 2.2	2.95 ± 0.12	4.1%

Table 2: Location of the cosmogenic samples of site PD-02 within the depth profile and their major chemical concentrations relevant for the ^{36}Cl nuclide exposure dating. The full relevant chemical composition is presented in Table S1. All sampled individual clasts were composed of limestone. Reported uncertainties are within the 1σ range.

3.3.2. Sample preparation and measurements

The samples were mechanically cleaned, crushed and sieved to the 250-500 µm size fractions at the Geological Survey of Slovenia. The chemical treatment was performed at the University of Edinburgh (UK) using the protocol of Marrero et al. (2018). The concentration of ^{36}Cl and natural chlorine was measured via accelerator mass spectrometry (AMS) at the Cologne AMS facility (Tables 1 and S2). Within the same preparation and measurement cycle as the samples of PD-02, nine aliquots of the carbonatic interlaboratory calibration material CoCal-N (Mechernich et al., 2019) allow a direct quality control (Table S2). In order to calculate the specific production rate of ^{36}Cl of the samples along the depth profile, an aliquot of each AMS-measured fraction was analysed by ICP-OES at the University of Edinburgh. Additionally, major and trace element contents of bulk non-leached sample material were measured at Actlabs, Canada (Table S1).

3.3.3. Determination of ^{36}Cl ages

We computed the exposure age scenarios of the alluvial deposits by a depth profile using the Excel spreadsheet of Schimmelpfennig et al. (2009). The following ^{36}Cl production rates were integrated in the spreadsheet: 48.8 atoms ^{36}Cl (g Ca)$^{-1}$ a^{-1} for the spallation of calcium at sea level and high latitude (Stone et al., 1996 with scaling of Stone, 2000), spallation on K: 150 atoms ^{36}Cl (g K)$^{-1}$ a^{-1} (Marrero et al., 2016a), spallation on Ti: 13 atoms ^{36}Cl (g Ti)$^{-1}$ a^{-1} (Fink et al., 2000), spallation on Fe: 1.9 atoms ^{36}Cl (g Fe)$^{-1}$ a^{-1} (Stone, 2005), 245 atoms g^{-1} a^{-1} for the slow negative muon stopping rate (site-dependent value calculated from Marrero et al. 2016b), and 759 n cm^{-2} a^{-1} for production from low-energy neutron absorption from ^{35}Cl (Marrero et al., 2016a). For each sample, the resulting amounts of ^{36}Cl production by the major mechanisms are shown in Table S2. Topographic shielding corrections as well as the sample-specific attenuation length were determined using the CRONUS topographic shielding calculator (https://hess.ess.washington.edu/).

For specific scenarios of denudation rates and soil densities, the most likely exposure age scenarios and their corresponding pre-depositional ^{36}Cl concentrations were iteratively determined based on ^{36}Cl concentrations at the different subsurface depths of the samples (e.g., Frankel et al., 2007; Schmidt et al., 2011; Mechernich et al., 2018) (Table 4).

3.4. Electrical resistivity tomography (ERT)

In most rocks (and sediments) electrical conduction is mostly the consequence of pore fluids acting as electrolytes, with the actual mineral grains contributing very little to the overall conductivity (and its reciprocal resistivity) of the rock (Reynolds, 1997).The electrical conductivity of rocks and soils is clearly dependent on the amount of water in the medium, the conductivity of water and the way water is spread (porosity, the degree of saturation, cementation factor, fracturing) (Kowalczyk et al., 2014). Laboratory measurements of soil and sediment show high dependence of resistivity on the sample’s moisture content (degree of saturation) and porosity (e.g., Kowalczyk et al., 2014; Merritt et al., 2016). Hence, the different authors report different resistivity ranges for similar sediment bodies and bedrock, respectively (Table 3).

Lithology	**Resistivity (Ωm)**	**Reference**
Clay	up to 100	Ebraheem et al. (2013)
Clay	up to 50	Chambers et al. (2013)
Muddy sand	50–300	Pellicer and Gibson (2011), Chambers et al. (2013)
Gravelly muddy sand	50–400	Pellicer and Gibson (2011)
Gravelly sand	700–1200	Pellicer and Gibson (2011)
Sand and gravel	900	Chambers et al. (2013)
Sand and gravel	200–600	Chambers et al. (2011)
Gravel	300–1500	Beresnev, Hruby and Davis (2002)
Gravel	800–1500	Pellicer and Gibson (2011)
Saturated gravel	up to 150	Ebraheem et al. (2013)
Gravel (dry)	3000–6000	Ebraheem et al. (2013)
Fluvioglacial sand and gravel	700–1500	Chambers et al. (2011, 2013)
Fluvioglacial gravel, diamicton	100–1000	Pellicer et al. (2012)
Muddy diamicton	150–300	Pellicer and Gibson (2011)
Till	up to 1200	Dietrich and Krautblatter (2017)
Clayey till	~20	Chambers et al. (2011)
Limestone bedrock	1000–5000	Pellicer et al. (2012)
Limestone bedrock	1000–3000	Pellicer and Gibson (2011)
Limestone bedrock (dry)	up to 10000	Ebraheem et al. (2013)

Table 3. Published data on resistivity values of different lithologies.

To address our research objectives, we measured two 2-D ERT profiles in the Praprotna draga site (Figs. 2a and 6). Profile a (94 m length) was measured perpendicular to the direction of the moraine ridge in order to obtain the significant resistivity values and estimate the thickness of glacial deposits. Profile b (635 m in length) was measured in the longitudinal direction over the northernmost alluvial fan that starts on the slope (917 m a.s.l.) and ends in the depression (835 m a.s.l.), in order to determine the possible existence of other sedimentary bodies buried below the alluvial deposits and to obtain the overall thickness and spatial distribution of sediments. Profile b was not positioned in the straight line due to lush undergrowth, but along the forest pathway. Dipole-dipole and Wenner-Schlumberger arrays with 2 m electrode spacing were applied in Profile a, and dipole-dipole array with 5 m electrode spacing (roll-along technique) in Profile b. Two sections of the Profile b were also measured with 2 m electrode spacing, b1 (0–158 m, Wenner-Schlumberger array, roll-along technique) and b2 (dipole-dipole, 516–610 m) to provide a better resolution for the upper 18 m of the subsurface. All measured apparent resistivity pseudosections were inverted using the finite-element method (Silvester and Ferrari, 1990), with a difference between the model response and the observed data values reduced using the l1 norm smoothness-constrained Gauss-Newton least-squares optimization method, where the absolute difference (or the first power) between the measured and calculated apparent resistivity values is minimized (Claerbout and Muir, 1973), known also as a blocky inversion method (Loke et al., 2003). A small cut-off factor was applied on the robust model constrain. The distribution of model cells is generated based on the sensitivity values (Jacobian matrix) of the model cells, which takes into account the information contained in the data set concerning the resistivity of the subsurface for a homogeneous earth model and tries to ensure that the data sensitivity of any cell does not become too small (Loke, 2013). Model refinement with a half width of one unit electrode spacing is used in all models. Joint inversion (Athanasiou et al., 2007) with dipole-dipole and Wenner-Schlumberger data sets was applied to the Profile a.

4. Results

4.1. Geomorphological and sedimentological characteristics

Praprotna draga is a large karst depression in the eastern part of Snežnik, which was modified by glacial and periglacial processes (Figs. 1b and 2a). We found that the area of the depression is 3.4 km^2 and the average diameter is ~ 2080 m. This 140 m deep depression has a minimum altitude of 780 m a.s.l. and its western slopes are characterized by undulated moraine morphology. Moraine ridges extend in the altitudinal range of 900-1290 m a.s.l. and are no more than 20 m high.

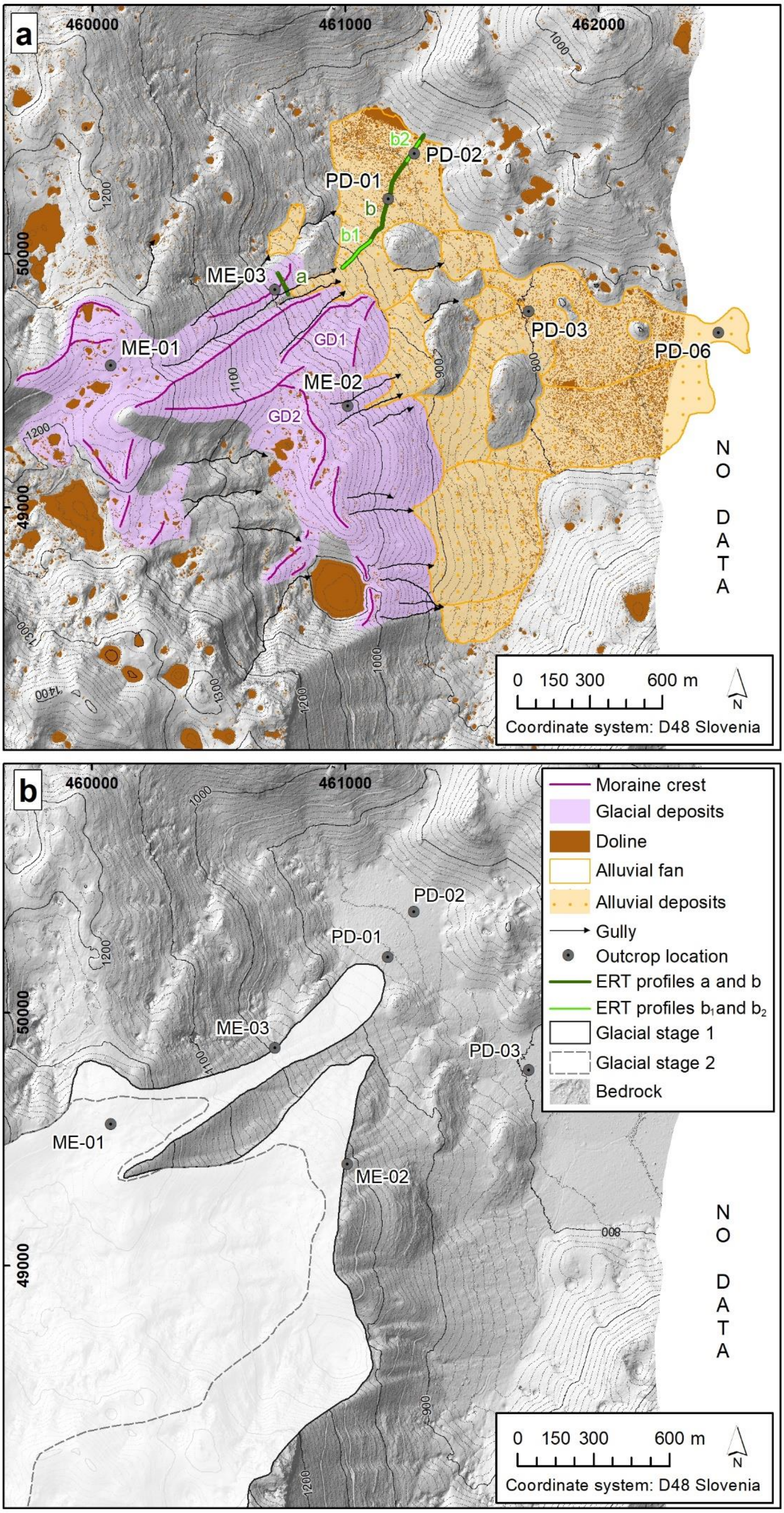
a
460000
461000
462000
50000
49000
PD-01
PD-02
PD-03
PD-06
ME-01
ME-02
ME-03
GD1
GD2
a
b
b1
b2
N O DATA
0 150 300 600 m
Coordinate system: D48 Slovenia
b
Moraine crest
Glacial deposits
Doline
Alluvial fan
Alluvial deposits
Gully
Outcrop location
ERT profiles a and b
ERT profiles b1 and b2
Glacial stage 1
Glacial stage 2
Bedrock

320

Fig. 2. (a) Glacial geomorphological map of Praprotna draga, including locations of sediment logging and ERT profiles. Doline areas were extracted from a 1 m DEM using the algorithm designed by Grlj and Grigillo (2014). GD1 and GD2 mark stratigraphically older and younger moraines, respectively. (b) Proposed extent of two glacial stages in the Praprotna draga depression, recognized on the basis of geomorphological, sedimentological and geophysical evidence.

We found that the upper-laying moraines (ME-01; Fig. 2a, Table 1) consist of a matrix-supported massive diamicton (Dmm) with subangular, polished and bullet-shaped clasts. The deposit becomes more clast-supported towards lower elevations and steeper slopes (ME-02 and ME-03; Table 1), where a matrix- to clast-supported massive to roughly stratified diamicton (Dmm-Dcs) dominates the composition of moraines. We observed a reduction in average and maximum clast size from 3–10 cm (max. 60 cm) in the ME-01 outcrop to 1–5 cm (max. 30 cm) in the ME-02 and ME-03 outcrops. Moreover, the clast roundness is greater heading towards the lower sections of moraines, where subangular to subrounded clasts prevail. Larger clasts commonly show greater modification in roundness. The soil thickness passes from 15 to max. 30 cm (Fig. 3). We performed clast lithological analysis in the ME-01 outcrop with the aim to identify a general provenance of sedimentary facies. Grey to dark-grey micritic laminated limestone of mudstone to wackestone textural types and locally dolomitized limestone prevails, suggesting typical Lower Cretaceous carbonate platform lithofacies. These are exposed in a wider area of the topmost parts of the Snežnik Mountain, W and SW of Praprotna draga (Šikić et al., 1972).

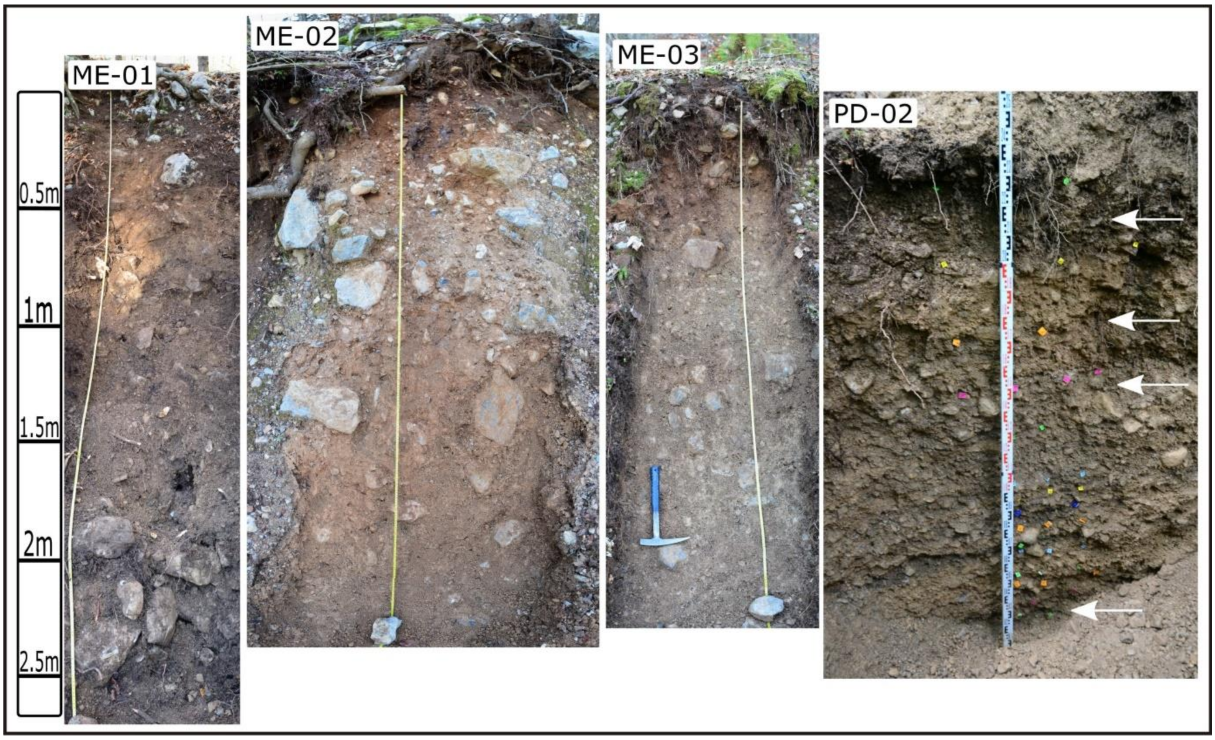

Fig. 3. Photos of till outcrops ME-01, ME-02, and ME-03, and the PD-02 sampling site in alluvial deposits. Flags of different colours indicate sedimentary boundaries within the profile PD-02. The sampled depth intervals are marked with white arrows. For location of the outcrops see Fig. 2 and Table 1.

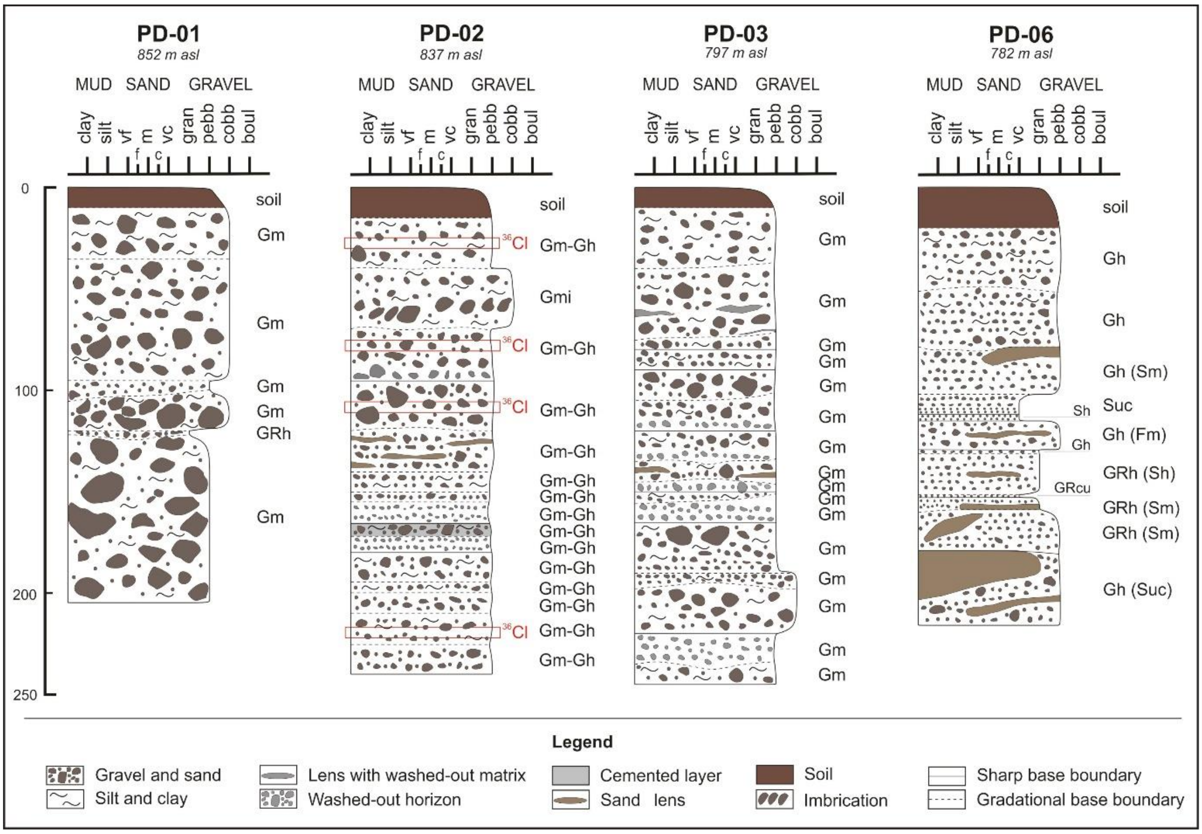

Fig. 4. Sedimentological logs of the trenches located in the alluvial fan. The ^{36}Cl sampled locations in PD-02 are marked with red dotted line square. For location of the trenches, see Fig. 2.

Below the moraines (>920 m a.s.l.), we mapped several alluvial fans that cover the western slopes and the entire floor of the depression, while some bedrock ridges crop out between them (Fig. 2). The southern fans are steeper in their proximal part (15-30°) from the northern fans (10-20°). They all merge towards east, where the mean gradient is 3-4°. Small dolines are present in the distal-most part of the fan area and at the contact with the eastern bedrock (limestone) slopes of the Praprotna draga depression. The formation of sufossion dolines in alluvial deposits indicates active karst processes.

The alluvial fans consist of stratified, poorly to moderately sorted, sub-angular to rounded gravels with occasional sand lenses (Fig. 4). The proximal fan zones (PD-

01; Table 1) are dominated by poorly sorted, moderately to well-rounded coarse-gravel facies consisting of massive to crudely bedded, clast-supported gravels (Gm), where gravel occupy between 70–90%, sand 0–15% and mud 0–30%. Towards the mid-fan zone (PD-02 and PD-03; Fig. 2a and Table 1) the gravel facies exhibit a marked downstream decline in the mean and maximum clast size, from 1–9 cm (max. 30 cm) to 0.2–6 cm (max. 5–15 cm). Poorly to moderately sorted, sub-angular to well rounded, massive to crudely horizontally bedded, clast supported gravels (Gm-Gh), where gravels occupy 70–95%, sand 0–30% and mud 0–15%, are interbedded with washed-out horizons and sparse sandy to silty lenses; lateral variations in facies type may occur due to the local channel network. The lower fan zone (PD-06; Fig. 2a and Table 1) is dominated by poorly to moderately sorted, sub-angular to rounded, horizontally bedded gravels (Gh) and granules (GRh), where gravels and granules occupy 50–100%, sand 0–50% and mud 0–40%, with common sandy to silty lenses (Sm-Fm). The average and maximum clast size is 0.1–1 cm and 5 cm, respectively. The soil thickness varies from 10–15 cm in the proximal (PD-01) and mid-fan zone (PD-02, PD-03) to 20 cm in the distal zone (PD-06). No buried palaeosoils have been detected within the profiles (Fig. 4). The lithological analysis of clasts from the PD-02 profile revealed a composition that matches the one of ME-01, suggesting local provenance from moraines and/or the wider area of the topmost parts of the Snežnik Mountain.

In addition to the geomorphological observations, the macroscopic sedimentological characterisation confirmed that the analysed PD-sediment sections were deposited in an alluvial environment. Proximal parts of alluvial fans are coarser grained and have thicker layers than distal parts, which is related to the rate of decline in gradient and consequential drop of transport energy, as typically observed in such depositional environment. Inverse grading and matrix-supported fabric have not been detected within the outcrops, thus we can exclude debris-flow origin. Based on resemblance (i.e. clasts lithological composition, shape and size) between glacial sediments described in moraines and alluvial sediments laying on the slopes bellow the moraines, we interpret that the glacial sediments were the origin for alluvial sediments. Transport distance of alluvial deposits was thus relatively short, between several hundred meters to maximum 1.5 km. Clast roundness does not change significantly from moraines to alluvial sediments, which supports the hypothesis that the transport was short. Geometrical relationships between individual alluvial fans, which are visible at the surface (Fig. 2a), suggest there were multiple pulses of alluvial fan formation. However, based on sedimentological sections alone, the individual events could not be distinguished. The alluvial fan formation process was nevertheless continuous without longer periods of inactivity that would allow soil formation, as suggested by the absence of buried paleosoils within investigated sections. Similar thicknesses of soil cover in all investigated sections imply the alluvial fans seem to be deposited at roughly the same time.

4.2. ^{36}Cl exposure age

Specific details of the cosmogenic samples in profile PD-02 are summarized in Tables 2 (resulting chlorine concentrations), S1 (chemical sample composition) and S2 (details of the sample preparation and measurement). All four samples have a similar chemical composition with 51.3–54.6% of CaO (Table S1) and moderately high stable chlorine concentrations (47.3–49.6 µg g^{-1}, Table 2). This indicates that spallation is the main production of ^{36}Cl and that thermal neutron production has a significant contribution to the total production (5-25% depending on the depth of the sample, Table S2). The measured ^{36}Cl concentrations decrease with depth from

$5.11 \pm 0.23\ 10^5$ atoms g^{-1} to $2.61 \pm 0.12\ 10^5$ atoms g^{-1} for the upper three samples and the ^{36}Cl concentration of the lowermost sample CRN PD-02/215-220 cm is with $2.95 \pm 0.12\ 10^5$ atoms g^{-1} slightly higher than the sample at 105–110 cm depth. The ^{36}Cl and natural Cl concentration measurements of the standard material CoCal-N are in a good agreement with the values obtained from other laboratories (Mechernich et al., 2019).

	Denudation rate (mm ka^{-1})	Inheritance ^{36}Cl (10^5 atoms g^{-1})	Modelled ^{36}Cl conc at surface (10^5 atoms g^{-1})	Modelled age of deposition (ka)
Soil density 2.1 g cm^{-3}				
Scenario 1	0	0.61 ± 0.29	5.8 ± 0.7	11.0 ± 1.3
Scenario 2	10	0.62 ± 0.29	6.0 ± 0.7	11.6 ± 1.4
Scenario 3	**20**	**0.63 ± 0.32**	**6.2 ± 0.6**	**12.3 ± 1.7**
Scenario 4	30	0.66 ± 0.38	6.3 ± 0.5	13.3 ± 2.0
Scenario 5	40	0.59 ± 0.40	6.4 ± 0.4	14.8 ± 2.8
Scenario 6	50	0.53 ± 0.45	6.5 ± 0.4	17.0 ± 4.0
Scenario 7	60	0.46 ± 0.46	6.5 ± 0.4	20.4 ± 6.7
Soil density 1.9 g cm^{-3}				
Scenario 8	0	0.32 ± 0.31	5.6 ± 0.7	11.2 ± 1.2
Scenario 9	20	0.38 ± 0.27	6.0 ± 0.5	12.4 ± 1.4
Soil density 2.3 g cm^{-3}				
Scenario 10	0	0.63 ± 0.57	5.8 ± 0.6	10.5 ± 1.4
Scenario 11	20	0.63 ± 0.57	6.3 ± 0.5	12.0 ± 1.7

Table 4. ^{36}Cl modelling estimates for different scenarios of soil density and denudation rates. Topographic shielding is 0.9852. No snow and vegetation shielding was applied. The modelled depth profiles of scenario 1 and 3 (bold) are shown in Fig. 5.

The sediment density was estimated to 2.1 g cm^{-3} according to typical values of dry unit weight of poorly graded gravel, sandy gravel, with little or no fines (Geotechdata.info). Similar estimations for the density of alluvial deposits have also been determined elsewhere (e.g., Machette et al., 2008; Moulin et al., 2016). The influence of different denudation rates on the age calculations of alluvial deposit was tested by using rates between 0 mm ka^{-1} and 60 mm ka^{-1} in steps of 10 mm ka^{-1} (Table 4). These cover a range of the northern Mediterranean limestone lowering rates (e.g., Cucchi et al., 1995; Plan, 2005; Furlani et al., 2009; Levenson et al., 2017; Thomas et al., 2018).

The most likely exposure age of the alluvial deposit was computed based on an iterative adaption of the pre-depositional (inherited) ^{36}Cl concentration and exposure age. This adaption aimed that all four data points lie on the theoretical depth profile when accounting for the 1σ uncertainties of both the data points and the ^{36}Cl production rates (Fig. 5). All depth profiles indicate that the ^{36}Cl concentration of the lowermost sample CRN PD-02/215-220 cm is too high compared to the ^{36}Cl concentration of the other three samples (Fig. 5). Hence, it was excluded from the curve fitting. The resulting depth profiles lead to a minimum age of the alluvial deposit of 11.0 ± 1.3 ka when assuming no denudation up to an age of 13.3 ± 2.0 ka for a likely rate of 30 mm ka^{-1} of denudation. For higher denudation rates the modelled ages and age uncertainties get significantly higher, e.g., 20.4 ± 6.7 ka for 60 mm ka^{-1} of denudation (Table 4). Age uncertainties related to the influence of different soil densities are negligible compared to the uncertainties related to the ^{36}Cl concentration measurements or the denudation rates.

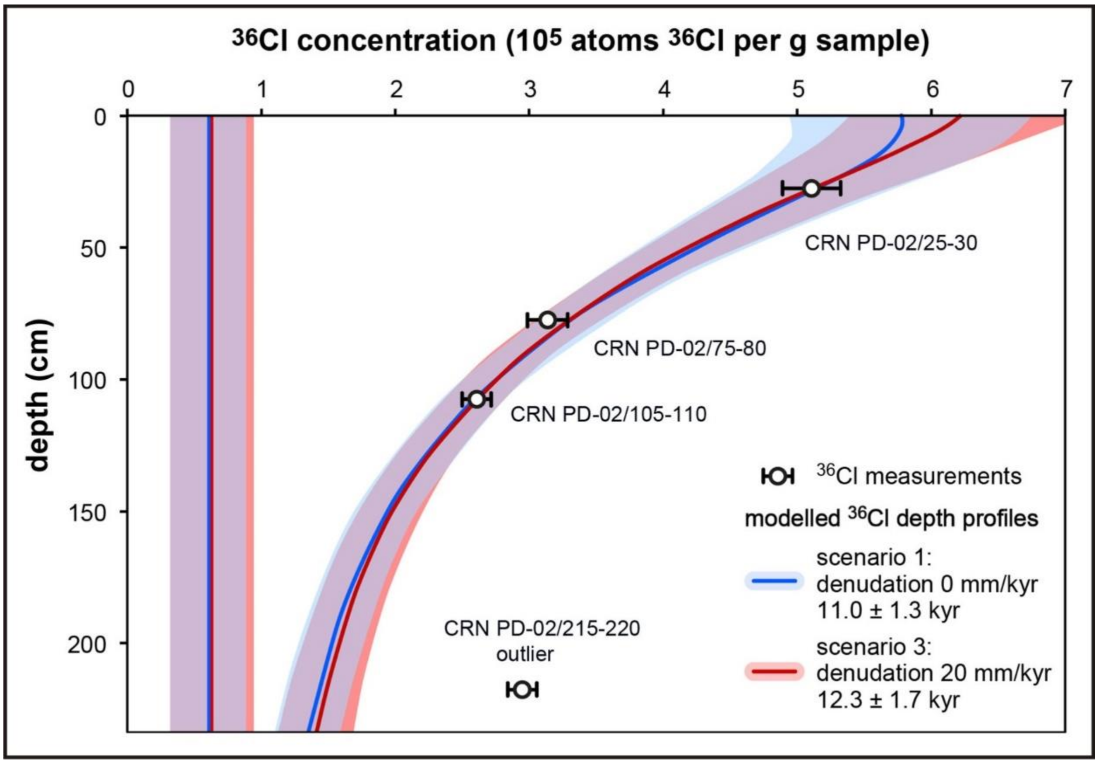

Fig. 5. ^{36}Cl concentration as a function of depth on the alluvial fan at site PD-02. Data points (circles) are derived from the amalgamated limestone pebble samples (Table 2). The (1σ) analytical uncertainties in ^{36}Cl concentration were incorporated in the model optimization. The modelled ^{36}Cl depth profiles of the ^{36}Cl concentration of the tested scenarios are similar (Table 4) and for better overview, we show only the exposure model optimization using denudation rates of 0 (blue) and 20 mm ka^{-1} (red) and a soil density of 2.1 g cm^{-3}. The vertical line with its uncertainty represents the hypothetical pre-depositional ^{36}Cl component and the exponential curved represents the modelled total concentration.

4.3. Inverse ERT models

The resistivity distribution of the inverse ERT models shows well-contrasted resistivity bodies that are being described in terms of geological layers based on the geomorphological and sedimentological characterization of the study area and representative resistivity ranges for similar rocks/sediments (Table 3).

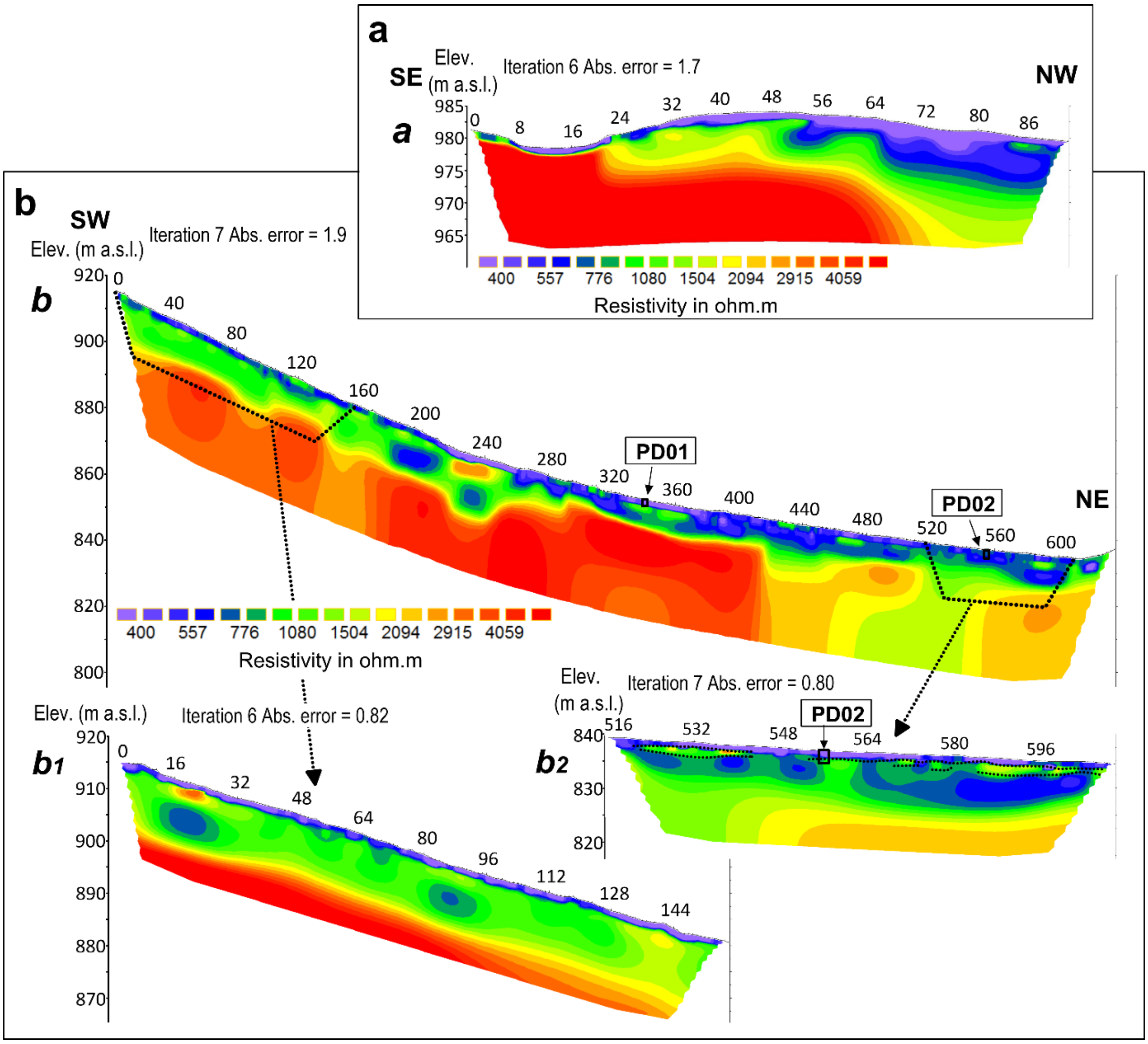

Fig. 6. Inverse ERT models of (a) Profile a and (b) Profile b with higher resolution sections b_1 and b_2 (occasionally washed out horizon is marked with black dotted line). Distance is shown in meters on the top of each profile.

4.3.1. Profile a (Figs. 2a and 6a)

The low resistivity area (200–900 Ωm) with thickness up to ~8 m at the top of the profile, corresponds to the glacial deposits described in the outcrop ME-03 (Figs. 2 and 3), located ~50 m to the SW of Profile a. The medium (900–1500 Ωm) resistivity body with thickness up to ~6 m (and depth up to ~14 m) located below, might either correspond to the same, but coarser and/or less saturated glacial deposits, or even to the stratigraphically older glacial deposits. In the latter case, the relatively higher resistivity values could be due to a higher degree of cementation, resulting in lower porosity and lower moisture content. The highest resistivity body (3000–6000 Ωm) in the lower part of the ERT image corresponds to the solid limestone bedrock, which crops out on the SE side of the profile and is buried below glacial deposits towards NW. The relatively high resistivity corrugated area (1500–2000 Ωm) overlying the limestone bedrock reflects glacially reshaped bedrock with fissured and weathered limestone.

4.3.2. Profile b (Fig. 2a and 6b)

The highest resistivity area (2500–6000 Ωm) corresponds to the limestone bedrock, wherein subvertical fault is likely present at ~160 m of the profile distance (at the area of 2500 Ωm). Bedrock lies between ~7 m and 20 m below the surface, having an undulated shape in the first 280 m of the profile length. The low resistivity (sub)vertical zone within the bedrock (1500–2500 Ωm) starts at 420 m of the profile length and continues to the end of the profile, indicating a fault zone is present in the limestone bedrock.

The top layer with lower resistivity (200–900 Ωm, locally 1000 Ωm) along the whole Profile b belongs to deposits consisting of coarse-gravel facies (PD-01 and PD-02 in Fig. 4).The thickness (and depth) of these sediments amounts to ~2 m in the first 260 m of the profile distance, and 5–10 m at lower altitudes. The higher resistivity interrupted layer of up to ~1000–2000 Ωm that can be observed at higher resolution section b_2 (marked with black dotted line in Fig. 6b-b_1) within a relatively homogenous resistivity body can be explained in terms of coarser sediment and/or washed out horizon, described at the bottom of the PD-02 profile. It might also indicate the boundary between younger and older alluvial deposits.

Two relatively homogenous medium resistivity areas (900–1500 Ωm) are present between bedrock and near-surface low resistivity alluvial deposits. The first is positioned on the SW slope and the second lies on the NE side of the Profile b above the bedrock fault zone. The first medium resistivity body (900–1500 Ωm) above the bedrock is relatively homogenous in the first 180 m of the profile distance, with average thickness of ~10–12 m. This continues along the profile to a less homogenous section at 180–280 m of the profile distance with two lower resistivity areas (~600 Ωm) and one higher resistivity block (~2500 Ωm). However, a bigger portion of the area still reaches resistivity values of 900–1500 Ωm, thus it can be considered as a relatively uniform sediment body with local resistivity abruptions. A sharp resistivity transition (2.5 to 5 fold) to the underlying limestone bedrock clearly separates the whole sequence from the bedrock. According to the vicinity of outcropping glacial deposits (Fig. 2a), the described sediment body likely represents coarser (and less saturated) or even cemented glacial deposits, resulting in higher resistivity values with respect to the glacial deposits present at the surface of the Profile a. The whole section might correspond to alluvial deposits if we consider that the bottom resistivity of PD-01 and PD-02 trenches reaches up to 1000 Ωm and the fact that the proximal part of alluvial fans are coarser grained and have thicker layers than distal parts. However, this interpretation is less likely.

The second area having similar resistivity values (900–1500 Ωm) is largely situated above the fault zone with thickness up to ~8 m (and reaching depth up to ~15 m). Based on resistivity values and its superposition it likely represents stratigraphically older alluvial deposits.

5. Discussion

5.1. Subsurface stratigraphy

Based on ERT results, we propose two interpretations in terms of different stratigraphy of the medium resistivity bodies, while bedrock (B), fault zone (B-FZ) and fractured bedrock (B-FW) remain the same in both interpretations. The first interpretation (Fig. 7a) is consistent with the geomorphological and sedimentological data observed on the field, while the second interpretation (Fig. 7b) is furthermore consistent in terms of similarities in resistivity ranges. However, the GD0 sediment body in the second interpretation cannot be associated with any of the mapped geomorphological features on the surface.

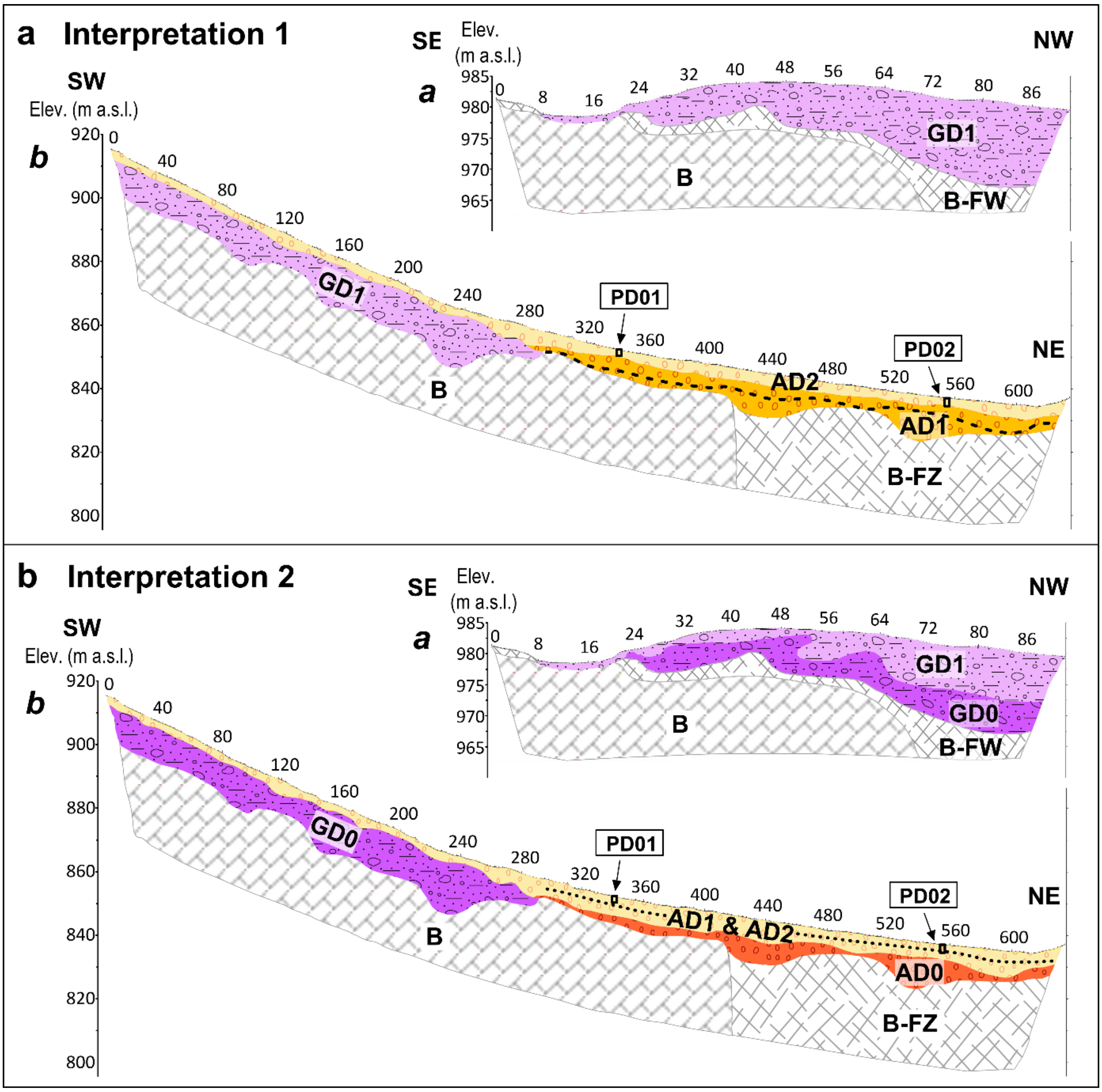

Fig. 7. The two most probable interpretations of the ERT models: a) Interpretation 1, and b) Interpretation 2. Distance (in meters) is shown on the top of each profile. B – limestone bedrock, B-FZ – fault zone in limestone bedrock, B-FW – fractured and/or weathered bedrock, GD0 – oldest glacial deposits related to pre – LGM glaciation, GD1 – older glacial deposits related to LGM, AD0 – alluvial deposits related to GD0, AD1 – alluvial deposits related to GD1, AD2 – youngest alluvial deposits (dated to Younger Dryas).

5.1.1. Interpretation 1

In Profile a, the whole resistivity range of 200–1500 Ωm, with thickness up to ~14 m, is interpreted as the glacial deposit GD1 observed in the ME-03 outcrop. The same interpretation was made for the ~10–12 m thick buried sediment body in the first 280 m of the Profile b (900–1500 Ωm), which is a continuation of the right lateral moraine, located 10 m higher and 70 m further towards SW. Slightly higher resistivity values of GD1 in Profile b with respect to GD1 in Profile a can be related to a decreasing amount of matrix towards palaeo-ice margin, where till deposits gradually pass over to alluvial deposits, which is also supported by our observations from several outcrops (Figs. 3 and 4). Variable resistivity values within both GD1 sediment bodies are likely a result of local differences in saturation and clast size.

The whole surface of the Profile b is covered by the youngest alluvial deposits AD2 (200–900 Ωm, locally 1000 Ωm), observed in the PD-01 and PD-02 trenches. These overlay glacial deposits GD1 in the first 280 m of the profile and stratigraphically older alluvial deposits AD1 in the rest of the profile. While the boundary between GD1 and AD2 is well justified with the differences in resistivity, it is more difficult to depict the boundary between AD1 and AD2. One possibility is to place the boundary at the highest contrast in resistivity values between the lower (900–1500 Ωm) and upper (200–900 Ωm, with thin interrupted layer ~1000–2000 Ωm) alluvial deposits (marked with black dashed line on Profile b in Fig. 7a). This would suggest that a difference in resistivity is due to the size of clasts, that is coarser in AD1 with respect to AD2, which can be explained by the distance from the palaeo-ice margin. Having the palaeo-ice margin marked with glacial deposits GD1, then AD1 can be considered as proximal, coarser alluvial deposits and AD2 as distal, finer alluvial deposits. According to this interpretation AD2 is concurrent with glacial deposits GD2 (Fig. 2a), and thus the difference in resistivity between AD1 and AD2 might as well be associated with a different degree of cementation and/or presence of washed-out horizons, which have been recognised in the PD-02 log (Fig. 4) within AD2 unit (section b_2 in Fig. 6b). Both conditions would result in higher resistivity values, since they would lead to reduced moisture content in sediments, common for high altitude karst environment, where vertical drainage and consequently no broader long-term saturation zones are present. In this hypothesis the thickness (and depth) of AD1 is up to 10 m, while the thickness and depth of AD2 is up to 8 m and 15 m, respectively.

An alternative boundary between AD1 and AD2 (marked with lighter and darker yellow colour on Profile b in Fig. 7a) can be depicted at the depth of the lowermost sample in PD-02, recognized as an age outlier. This sample most probably belongs to an older depositional event and hence experienced longer exposure history, resulting in the relatively high ^{36}Cl concentration, which does not fit into the depth profile curve (Fig. 5). This cannot be directly supported with the results of the sedimentological analyses since no erosional discontinuities were detected within the outcrop. However, washed-out and occasionally cemented horizons at a depth of 155–180 cm in PD-02 (Fig. 4) indicate a likely short interruption in deposition and thus a boundary between two events. This interpretation is supported by obvious vertical changes of resistivity values in alluvial deposits on the higher-resolution ERT section b_2, where thin higher resistivity layer (~1000–2000 Ωm) is present at a depth interval of ~1.5–3 m (marked with black dotted line in section b_2 of Fig. 6b), within the layer otherwise characterized by resistivity values of 200–900 Ωm. In this case, the higher resistivity values indicate occasionally washed-out horizons within alluvial deposits. The thin higher resistivity layer is also laterally discontinuous, suggesting the channel-network formation. The thickness (and depth) of AD2 according to this interpretation is up to 3 m, and the thickness and depth of AD1 is up to 12 m and 15 m, respectively.

5.1.2. Interpretation 2

Interpretation 2 associates higher resistivity values (900–1500 Ωm) of the GD1 and AD1 sediment bodies in the interpretation 1 with higher degree of sediment cementation. These sections are marked with GD0 and AD0 in Fig. 7b and are in a stratigraphically older position from GD1 and AD1. This implies GD0, not visible on the surface, points to a larger glacier extent from GD1, which is now present only as top layer in Profile a with resistivity values of 200–900 Ωm and thickness up to ~8 m. In this interpretation, the alluvial deposits AD0 have the same resistivity range as glacial deposits GD0 (900–1500 Ωm) and reach thickness and depth up to ~8 m and ~15 m, respectively. GD0 in Profile a show severely undulated surface, suggesting they were subglacially deformed. The thickness of GD0 reaches up to ~6 m in Profile a and ~10–12 m in Profile b.

Again, the border between AD1 and AD2 (marked with black dotted line on Profile b in Fig. 7b) is not entirely clear. This border is associated with the depth of the age outlier and washed-out horizons in the PD-02, supported by anomalous higher resistivity layer on section b_2. Thus, AD1 has resistivity values in the range of 500–900 Ωm, with an exception of laterally discontinuous washed out horizons, having values of ~1000–2000 Ωm. In this interpretation, the thickness of AD0 is up to 8 m, for AD1 up to 4 m and for AD2 up to 3 m.

5.2. Uncertainties and assumptions of the cosmogenic ^{36}Cl exposure age

Cosmogenic ^{36}Cl nuclide dating modelling estimate suggests an age of 12.3 ± 1.7 ka (1σ) as the most probable age of the dated alluvial deposits (PD-02 within the AD2 unit) in the Praprotna draga depression by using 2.1 g cm^{-3} for a density of deposits and 20 mm ka^{-1} for a denudation rate. Both parameters were estimated and considered as most probable using previously published data and taking into account the local characteristics. Although the density of coarse-grained deposits is difficult to determine accurately, a variation of ± 0.2 g cm^{-3} change the exposure age only by ± 0.3 ka.

The study area is characterized by high MAP (>2500 mm) and the dominant lithology of the dated clasts is Cretaceous limestone. These lithological and climate characteristics are roughly similar to those in the Classical Karst area, where the mean limestone bedrock lowering rate of 18 mm ka^{-1} was measured within a period of up to 26 years using micro-erosion meter (Furlani et al., 2009). Even higher denudation rates (30–60 mm ka^{-1}) were measured on the exposed carbonate bedrock in SE France (Thomas et al., 2018) and elsewhere in the Mediterranean (Levenson et al., 2017 and references therein). Denudation rates determined on Mediterranean and central European sediments also vary distinctly and appear to be within similar range (10–80 mm ka^{-1}; e.g., Siame et al., 2004; Ryb et al., 2014; Ruszkiczay-Rüdiger et al., 2016a). Nevertheless, our study area receives more precipitation than the nearby Classical Karst (MAP: 1340 mm; Furlani et al., 2009) and the material is not bedrock but alluvial material, which both suggest that the denudation rate is likely to be higher.

The age modelling does not consider a correction for snow shielding, although the continental climate and the high precipitation imply a substantial snow cover in the study area. This is related to the difficult quantification of the effect of the snow cover, since on one hand the snow cover reduces the production of the target elements, but on the other hand the hydrogen rich cover increases the production rate based on thermal neutrons. This rate can get significant in the case of the moderate concentrations of stable Cl in the samples (Dunai et al., 2014; Gromig et al., 2018).

It is clear from Table 4 that applying a range of relevant denudation rates for correcting exposure ages will have a great impact on the correct age of the landform. For example, if different estimates of soil density and denudation are used, the resulting age falls within a range of ~ 9–21 ka (1σ uncertainties), which will shift our most likely age interpretation from Younger Dryas to Holocene, Oldest Dryas or even LGM. The impact of other published ^{36}Cl production rates (e.g., Marrero et al., 2016b), or the inclusion of estimates of snow or vegetation interactions is negligible within the 1σ age range.

5.3. Time frame from glacial to non-glacial conditions

Based on the distribution of glacial deposits on the surface in the Praprotna draga hinterland and their morphological expression (Fig. 2a), at least two glacial phases with an altitudinal difference in glacier fronts of ~140 m can be distinguished. Glaciers in the older phase (Glacial stage 1 in Fig. 2b) almost reached the bottom of the depression at 860–910 m a.s.l., while in the younger phase (Glacial stage 2 in Fig. 2b) they retreated back to ~1050 m a.s.l. The two-phase interpretation is also supported by the Interpretation 1 of the ERT models (Fig. 7a) performed along the northernmost alluvial fan, which show a diamicton-like sedimentary body (GD1) buried below alluvial deposits (AD2). This is the most probable interpretation of the ERT models, because it is well supported with the observed geomorphological and sedimentological data in the study area. An alternative explanation, based only on the Interpretation 2 of the ERT models (Fig. 7b) suggests that GD1 in Interpretation 1 are in fact older GD0 glacial deposits that do not correlate with any of the mapped moraines on the surface. They might belong to an older and slightly larger glaciation from Glacial stage 1. Although the exact timeframe of glacial phases is still unknown, we can make some assumptions about their age by taking into account the equilibrium line altitudes (ELAs) estimated for the neighbouring past glacierized areas and based on the correlation with the results from the nearby Gomance area (Fig. 1).

The equilibrium line altitude (ELA) for the Glacial stage 1 glaciers was calculated by Žebre (2015) to 1325-1282 m using a range of representative modern area altitude balance ratios (AABR) of 1.5-3.5 (Osmaston, 2005; Rea, 2009) and 1324 m by applying the accumulation-area ratio (AAR) of 0.6. Similarly low ELAs were estimated for the largest, tentatively Last glaciation for the nearby Julian Prealps (ELA ~1130-1200 m) (Monegato, 2012) and for the Trnovski gozd plateau (ELA ~1255-1216 m) (Žebre et al., 2013) using the AABR method. Low ELA values (ELA ~1256 m) in the Balkans were calculated using the AAR of 0.8 only for the glaciers dated to MIS 12 in the coastal Orjen Mountain (Montenegro) receiving high modern MAP (~5000 mm), while during the Last glaciation the ELA was calculated to 1456 m using AAR of 0.5 (Hughes et al., 2010). The minimum ELAs estimated for other mountains in the Balkans that are located more inland, were substantially higher (ELA ~1600-2200 m) (e.g., Kuhlemann et al., 2009, 2013; Hughes et al., 2011; Ribolini et al., 2011). This suggests that a correlation with the Snežnik Mountain is less reasonable. Based on ELA correlations and the stratigraphic relationship with the deposits filling the Gomance karst depressions (see Introduction and references therein), the Glacial stage 1 can be potentially linked to the Last glaciation, although an older age is not to be excluded, as suggested by other studies in the Balkan Peninsula (e.g., Hughes et al., 2006, 2010, 2011). The latter is a more likely explanation for the GD0 glacial deposits if considering the Interpretation 2 of subsurface stratigraphy as being correct. However, estimating the ELA for the younger, Glacial stage 2, is subject to more uncertainties, because at that time Snežnik was still covered with an ice field, hence its extent is difficult to determine owing to karst topography and missing geomorphological evidence in some places. Assuming the Glacial stage 1 belongs to the LGM, then the Glacial stage 2 can be associated with the first recessional phase after the LGM (e.g., Oldest Dryas; ca. 17.5–14.5 ka). It is unlikely that the Glacial stage 2 would belong to the Younger Dryas (YD) phase (12.9–11.7 ka). Based on the findings from other studies in the Balkans, (e.g., Kuhlemann et al., 2009; Hughes et al., 2010; Ribolini et al., 2011; Pope et al., 2015), the YD ELA was on average 180 m higher with respect to the LGM ELA. In the Alps, the YD-LGM differences in ELA were even greater (> 650 m) (Ivy-Ochs, 2015). Applying the average-recorded YD-LGM ELA difference to Snežnik results in the YD ELA of ~1500 m. An ELA at this high altitude suggests that the accumulation area would be too small for glaciers to reach down to 1050 m a.s.l., where the Glacial stage 2 moraines are deposited. The YD glaciation in the form of small cirque glaciers was established on five mountain massifs in the Balkans (see Introduction section) but cannot be confirmed on Snežnik, which is in agreement with the findings from the Pelister Mountain (Macedonia) (Ribolini et al., 2018). Here we propose that the dated and also the youngest alluvial deposits (i.e. the uppermost ~2 m within AD2 stratigraphic unit) in Praprotna draga were not deposited directly by meltwaters, although the cosmogenic dating of the PD-02 depth profile suggests they were deposited during the YD cooling at 12.3 ± 1.7 ka. Hence, we can assume that the youngest deposition took place some thousands of years after the glacier retreat during the transition period from glacial to non-glacial conditions, when the slope denudation and remobilization of pre-existing glacigenic sediments reinitiated fan aggradation. Our findings suggest that the time window of paraglacial adjustment in Snežnik was brief and that it ended in YD, which is unlike in the adjacent SE Alps, which are still recovering from the Last glaciation and undergoing paraglacial sediment reworking also in the present climate (Bavec et al., 2004; Bavec and Verbič, 2011). A short-lived paraglacial period, explained by a quick expansion of dense forest and subsequent stabilization of deglaciating terrain has been suggested also for other Mediterranean mountains (Woodward et al., 2014; Delmas et al., 2015).

We therefore argue that a brief paraglacial response to the last deglaciation was not only conditioned by the quick expansion of dense forest (Woodward et al., 2014), but also by the inefficient surface runoff on deglaciated karst terrain. During glacial advances, surface runoff prevailed towards glacier margins and karst depressions received large sediment fluxes from meltwaters. In the course of deglaciation, a subterranean drainage started to prevail due to exposed limestone bedrock areas and reduced sediment load, favouring the quick adjustment of relief to non-glacial conditions and preservation of sediment fill. At present, the dominant pathway for runoff is the karst network and the chemical weathering of the surface is the main process in the study area, while slope processes are mainly limited to steep slopes and/or mechanically less resistant lithology. This results in almost negligible sediment supply, leaving the fans inactive at present and their surfaces well vegetated.

6. Conclusions

We studied a well-preserved sediment infill of the Praprotna draga karst depression in the deglaciated Snežnik Mountain (Slovenia) by applying various methods, such as geomorphological mapping, sediment facies analysis, ERT measurements and cosmogenic ^{36}Cl nuclide exposure dating. According to the Interpretation 1 of ERT models, which is well supported by geomorphological and sedimentological data, we divided subsurface stratigraphy in glacial (GD1) and alluvial deposits (AD1), associated with the LGM and buried by alluvial deposits (AD2), linked to Late-glacial. The topmost ~2 m of AD2 was dated to the Younger Dryas cooling at 12.3 ± 1.7 ka. The existence of the Younger Dryas glaciers in Snežnik is unlikely based on the equilibrium line altitude reconstructions, hence we propose that the youngest alluvial deposits of the Late-glacial aggradation phase (AD2) relate with the paraglacial period that ended in Younger Dryas. Our findings suggest that the time window of paraglacial adjustment in Snežnik was short, and it depended largely on the karst geomorphic system and quick vegetation change. We also demonstrate that the sediment supply in karst areas during glacial and paraglacial periods contrast sharply with present-day conditions, owing mainly to a change in the type of drainage (surface versus underground). Our results are subject to uncertainty because of some assumptions regarding the exact time of glacier retreat. Therefore, further work on the age of glacier stabilization and improvement of the alluvial fan chronology is needed.

Acknowledgements

This work was financed by the Slovenian Research Agency (research core funding No. P1-0011 and P1-0025). We acknowledge field assistance of Eva Mencin Gale, Blaž Milanič and Anže Markelj from the Geological Survey of Slovenia, and Janez Sevšek from the Department of Geology, University of Ljubljana. We are thankful to two anonymous referees for their constructive comments and suggestions that improved the manuscript. We also thank Adina E Racoviteanu for her help with the English revision of the paper.

References

Adamson, K.R., Woodward, J.C., Hughes, P.D., 2014. Glaciers and rivers: Pleistocene uncoupling in a Mediterranean mountain karst. Quat. Sci. Rev. 94, 28–43. https://doi.org/10.1016/j.quascirev.2014.04.016

Athanasiou, E.N., Tsourlos, P.I., Papazachos, C.B., Tsokas, G.N., 2007. Combined weighted inversion of electrical resistivity data arising from different array types. J. Appl. Geophys. 62, 124–140. https://doi.org/10.1016/j.jappgeo.2006.09.003

Ballantyne, C.K., 2002. Paraglacial geomorphology. Quat. Sci. Rev. 21, 1935–2017. https://doi.org/https://doi.org/10.1016/S0277-3791(02)00005-7

Ballantyne, C.K., 2003. Paraglacial landform succession and sediment storage in deglaciated mountain valleys: theory and approaches to calibration. Zeitschrift für Geomorphol. Suppl. 132, 1–18.

Bavec, M., Verbič, T., 2011. Glacial history of Slovenia, in: Horne, D.J., Holmes, J.A., Rodriguez-Lazaro, J., Viehberg, F.A. (Eds.), Developments in Quaternary Science. pp. 385–392. https://doi.org/10.1016/B978-0-444-53447-7.00029-5

Bavec, M., Tulaczyk, S.M., Mahan, S.A., Stock, G.M., 2004. Late Quaternary glaciation of the Upper Soča River Region (Southern Julian Alps, NW Slovenia). Sediment. Geol. 165, 265–283. https://doi.org/10.1016/j.sedgeo.2003.11.011

Braucher, R., Merchel, S., Borgomano, J., Bourlès, D.L., 2011. Production of cosmogenic radionuclides at great depth: A multi element approach. Earth Planet. Sci. Lett. 309, 1–9. https://doi.org/10.1016/j.epsl.2011.06.036

Ćalić, J., 2011. Karstic uvala revisited: Toward a redefinition of the term.

Geomorphology 134, 32–42. https://doi.org/10.1016/J.GEOMORPH.2011.06.029

Church, M., Slaymaker, O., 1989. Disequilibrium of Holocene sediment yield in glaciated British Columbia. Nature 337, 452. https://doi.org/10.1038/337452a0

Claerbout, J.F., Muir, F., 1973. Robust modeling with erratic data. Geophysics 38, 826–844.

Colucci, R.R., 2016. Geomorphic influence on small glacier response to post-Little Ice Age climate warming: Julian Alps, Europe. Earth Surf. Process. Landforms 41, 1227–1240. https://doi.org/10.1002/esp.3908

Colucci, R.R., Boccali, C., Žebre, M., Guglielmin, M., 2016. Rock glaciers, protalus ramparts and pronival ramparts in the south-eastern Alps. Geomorphology 269, 112–121. https://doi.org/10.1016/j.geomorph.2016.06.039

Cordier, S., Adamson, K., Delmas, M., Calvet, M., Harmand, D., 2017. Of ice and water: Quaternary fluvial response to glacial forcing. Quat. Sci. Rev. 166, 57–73. https://doi.org/10.1016/J.QUASCIREV.2017.02.006

Cucchi, F., Forti, F., Marinetti, E., 1995. Surface degradation of carbonate rocks in the Karst of Trieste (Classical Karst, Italy), in: Formos, J.J., Ginés, A. (Eds.), Karren Landforms. Palma, pp. 41–51.

Cvijić, J., 1893. Das Karstphänomen. Geogr. Abhandlungen 5, 218–329.

Delmas, M., Braucher, R., Gunnell, Y., Guillou, V., Calvet, M., Bourlès, D., 2015. Constraints on Pleistocene glaciofluvial terrace age and related soil chronosequence features from vertical 10Be profiles in the Ariège River catchment (Pyrenees, France). Glob. Planet. Change 132, 39–53.

https://doi.org/10.1016/J.GLOPLACHA.2015.06.011

Dunai, T., 2010. Cosmogenic Nuclides Principles, Concepts and Applications in the Earth Surface Sciences. Cambridge Academic Press, pp 198.

Dunai, T.J., Binnie, S.A., Hein, A.S., Paling, S.M., 2014. The effects of a hydrogen-rich ground cover on cosmogenic thermal neutrons: Implications for exposure dating. Quat. Geochronol. 22, 183–191. https://doi.org/10.1016/j.quageo.2013.01.001

Evans, D.J.A., Benn, D.I. (Eds.), 2004. A practical guide to the study of glacial sediments. Arnold, London. pp. 280.

Fink, D., Vogt, S., Hotchkis, M., 2000. Cross-sections for 36Cl from Ti at Ep=35–150 MeV: Applications to in-situ exposure dating. Nucl. Instruments Methods Phys. Res. Sect. B Beam Interact. with Mater. Atoms 172, 861–866. https://doi.org/10.1016/S0168-583X(00)00200-7

Frankel, K.L., Brantley, K.S., Dolan, J.F., Finkel, R.C., Klinger, R.E., Knott, J.R., Machette, M.N., Owen, L.A., Phillips, F.M., Slate, J.L., Wernicke, B.P., 2007. Cosmogenic 10Be and 36Cl geochronology of offset alluvial fans along the northern Death Valley fault zone: Implications for transient strain in the eastern California shear zone. J. Geophys. Res. Solid Earth 112, B06407. https://doi.org/10.1029/2006JB004350

Furlani, S., Cucchi, F., Forti, F., Rossi, A., 2009. Comparison between coastal and inland Karst limestone lowering rates in the northeastern Adriatic Region (Italy and Croatia). Geomorphology 104, 73–81. https://doi.org/10.1016/J.GEOMORPH.2008.05.015

Grlj, A., Grigillo, D., 2014. Uporaba digitalnega modela višin in satelitskega posnetka RapidEye za zaznavanje kraških kotanj in brezstropih jam Podgorskega krasa = Use of digital elevation model and RapidEye satellite image to locate karst depressions and unroofed caves of Podgorski. Dela 42, 129–147. https://doi.org/10.4312/dela.42.7.129-147

Gromig, R., Mechernich, S., Ribolini, A., Wagner, B., Zanchetta, G., Isola, I., Bini, M., Dunai, T.J., 2018. Evidence for a Younger Dryas deglaciation in the Galicica Mountains (FYROM) from cosmogenic 36Cl. Quat. Int. 464, 352–363. https://doi.org/10.1016/j.quaint.2017.07.013

Hancock, G.S., Anderson, R.S., Chadwick, O.A., Finkel, R.C., 1999. Dating fluvial terraces with 10Be and 26Al profiles: application to the Wind River, Wyoming. Geomorphology 27, 41–60. https://doi.org/https://doi.org/10.1016/S0169-555X(98)00089-0

Harbor, J., Warburton, J., 1993. Relative Rates of Glacial and Nonglacial Erosion in Alpine Environments. Arct. Alp. Res. 25, 1–7.

Hein, A.S., Hulton, N.R.J., Dunai, T.J., Schnabel, C., Kaplan, M.R., Naylor, M., Xu, S., 2009. Middle Pleistocene glaciation in Patagonia dated by cosmogenic-nuclide measurements on outwash gravels. Earth Planet. Sci. Lett. 286, 184–197. https://doi.org/https://doi.org/10.1016/j.epsl.2009.06.026

Hughes, P.D., Woodward, J.C., Gibbard, P.L., Macklin, M.G., Gilmour, M.A., Smith, G.R., 2006. The Glacial History of the Pindus Mountains, Greece. J. Geol. 114, 413–434. https://doi.org/10.1086/504177

Hughes, P.D., Woodward, J.C., van Calsteren, P.C., Thomas, L.E., 2011. The glacial history of the Dinaric Alps, Montenegro. Quat. Sci. Rev. 30, 3393–3412. https://doi.org/10.1016/j.quascirev.2011.08.016

Hughes, P.D., Woodward, J.C., van Calsteren, P.C., Thomas, L.E., Adamson, K.R., 2010. Pleistocene ice caps on the coastal mountains of the Adriatic Sea. Quat. Sci. Rev. 29, 3690–3708. https://doi.org/10.1016/j.quascirev.2010.06.032

Isotta, F.A., Frei, C., Weilguni, V., Perčec Tadić, M., Lassègues, P., Rudolf, B., Pavan, V., Cacciamani, C., Antolini, G., Ratto, S.M., Munari, M., Micheletti, S., Bonati, V., Lussana, C., Ronchi, C., Panettieri, E., Marigo, G., Vertačnik, G., 2014. The climate of daily precipitation in the Alps: development and analysis of a high-resolution grid dataset from pan-Alpine rain-gauge data. Int. J. Climatol. 34, 1657–1675. https://doi.org/10.1002/joc.3794

Ivy-Ochs, S., 2015. Glacier variations in the European Alps at the end of the last glaciation. Cuad. Investig. Geográfica 41, 295–315.

Kobal, M., Bertoncelj, I., Pirotti, F., Dakskobler, I., Kutnar, L., 2015. Using Lidar Data to Analyse Sinkhole Characteristics Relevant for Understory Vegetation under Forest Cover—Case Study of a High Karst Area in the Dinaric Mountains. PLoS One 10, 1–19. https://doi.org/10.1371/journal.pone.0122070

Komac, B., Hrvatin, M., Perko, D., Natek, K., Mihevc, A., Prelovšek, M., Zorn, M., Stepišnik, U., 2012. Recent Landform Evolution in Slovenia, in: Stankoviansky, M., Lóczy, D., Kotarba, A. (Eds.), Recent Landform Evolution: The Carpatho-Balkan-Dinaric Region. Springer, pp. 287–311.

Kowalczyk, S., Maślakowski, M., Tucholka, P., 2014. Determination of the correlation between the electrical resistivity of non-cohesive soils and the degree of compaction. J. Appl. Geophys. 110, 43–50. https://doi.org/10.1016/j.jappgeo.2014.08.016

Kranjc, A., 2010. Short History of Research, in: Mihevc, A., Prelovšek, M., Zupan Hajna, N. (Eds.), Introduction to the Dinaric Karst. Karst Research Institute at ZRC SAZU, Postojna, pp. 9–13.

Krklec, K., Domínguez-Villar, D., Perica, D., 2015. Depositional environments and diagenesis of a carbonate till from a Quaternary paleoglacier sequence in the Southern Velebit Mountain (Croatia). Palaeogeogr. Palaeoclimatol. Palaeoecol. 436, 188–198. https://doi.org/10.1016/J.PALAEO.2015.07.004

Kuhlemann, J., Gachev, E., Gikov, A., Nedkov, S., Krumrei, I., Kubik, P., 2013. Glaciation in the Rila mountains (Bulgaria) during the Last Glacial Maximum. Quat. Int. 293, 51–62. https://doi.org/10.1016/J.QUAINT.2012.06.027

Kuhlemann, J., Milivojević, M., Krumrei, I., Kubik, P.W., 2009. Last glaciation of the Šara Range (Balkan peninsula): Increasing dryness from the LGM to the Holocene. Austrian J. Earth Sci. 102, 146–158.

Levenson, Y., Ryb, U., Emmanuel, S., 2017. Comparison of field and laboratory weathering rates in carbonate rocks from an Eastern Mediterranean drainage basin. Earth Planet. Sci. Lett. 465, 176–183. https://doi.org/10.1016/j.epsl.2017.02.031

Loke, M.H., 2013. Tutorial : 2-D and 3-D electrical imaging surveys. Geotomo Softw. Malaysia 127.

Loke, M.H., Acworth, I., Dahlin, T., 2003. A comparison of smooth and blocky inversion methods in 2D electrical imaging surveys. Explor. Geophys. 34, 182–187, pp. 128.

Machette, M.N., Slate, J.L., Phillips, F.M., 2008. Terrestrial Cosmogenic-Nuclide Dating of Alluvial Fans in Death Valley, California. US Geol. Surv. Prof. Pap. 1–54.

Marjanac, L., Marjanac, T., Mogut, K., 2001. Dolina Gumance u doba Pleistocena. Zb. Društva za Povj. Klana 6, 321–330.

Marrero, S.M., Hein, A.S., Naylor, M., Attal, M., Shanks, R., Winter, K., Woodward, J., Dunning, S., Westoby, M., Sugden, D., 2018. Controls on subaerial erosion rates in Antarctica. Earth Planet. Sci. Lett. 501, 56–66. https://doi.org/10.1016/J.EPSL.2018.08.018

Marrero, S.M., Phillips, F.M., Borchers, B., Lifton, N., Aumer, R., Balco, G., 2016a. Cosmogenic nuclide systematics and the CRONUScalc program. Quat. Geochronol. 31, 160–187. https://doi.org/10.1016/j.quageo.2015.09.005

Marrero, S.M., Phillips, F.M., Caffee, M.W., Gosse, J.C., 2016b. CRONUS-Earth cosmogenic 36Cl calibration. Quat. Geochronol. 31, 199–219. https://doi.org/10.1016/j.quageo.2015.10.002

Mechernich, S., Dunai, T.J., Binnie, S.A., Goral, T., Heinze, S., Dewald, A., Schimmelpfennig, I. Keddadouche, K., Aumaître, G., Bourlès, D., Marrero, S., Wilcken, K., Simon, K., Fink, D., Phillips, F.M., Caffee, M.W., Gregory, L.C., Phillips, R., Freemann, S.P.H.T., Shanks, R.P., Sarıkaya, M.A., Pavetich, S., Rugel, G., Merchel, S., Akçar, N., Yesilyurt, S., Ivy-Ochs, S. Vockenhuber, C., 2019. Carbonate and silicate intercomparison materials for cosmogenic 36Cl measurements. Nucl. Instruments Meas. Phys. Res. B.

Mechernich, S., Schneiderwind, S., Mason, J., Papanikolaou, I.D., Deligiannakis, G., Pallikarakis, A., Binnie, S.A., Dunai, T.J., Reicherter, K., 2018. The Seismic History of the Pisia Fault (Eastern Corinth Rift, Greece) From Fault Plane Weathering Features and Cosmogenic 36Cl Dating. J. Geophys. Res. Solid Earth 123, 4266–4284. https://doi.org/10.1029/2017JB014600

Mercier, D., 2008. Paraglacial and paraperiglacial landsystems: concepts, temporal scales and spatial distribution. Géomorphologie Reli. Process. Environ. 14, 223–233. https://doi.org/10.4000/geomorphologie.7396

Merritt, A.J., Chambers, J.E., Wilkinson, P.B., West, L.J., Murphy, W., Gunn, D., Uhlemann, S., 2016. Measurement and modelling of moisture-electrical resistivity relationship of fine-grained unsaturated soils and electrical anisotropy. J. Appl. Geophys. 124, 155–165. https://doi.org/10.1016/j.jappgeo.2015.11.005

Mihevc, A., Prelovšek, M., 2010. Geographical position and general overview, in: Mihevc, A. (Ed.), Introduction to the Dinaric Karst. Karst Research Institute at ZRC SAZU, Postojna, pp. S6-8.

Milivojević, M., Menković, L., Ćalić, J., 2008. Pleistocene glacial relief of the central part of Mt. Prokletije (Albanian Alps). Quat. Int. 190, 112–122. https://doi.org/10.1016/j.quaint.2008.04.006

Ministry of the Environment and Spatial Planning Slovenian Environment Agency, n.d. LiDAR data Slovenia [WWW Document]. 2011. URL http://gis.arso.gov.si/evode/profile.aspx?id=atlas_voda_Lidar@Arso

Monegato, G., 2012. Local glaciers in the Julian Prealps (NE Italy) during the Last Glacial Maximum. Alp. Mediterr. Quat. 25, 5–14.

Moulin, A., Benedetti, L., Rizza, M., Jamšek Rupnik, P., Gosar, A., Bourlès, D., Keddadouche, K., Aumaître, G., Arnold, M., Guillou, V., Ritz, J.-F., 2016. The Dinaric fault system: Large-scale structure, rates of slip, and Plio-Pleistocene evolution of the transpressive northeastern boundary of the Adria microplate. Tectonics 35, 2258–2292. https://doi.org/10.1002/2016TC004188

Oliva, M., Žebre, M., Guglielmin, M., Hughes, P.D., Çiner, A., Vieira, G., Bodin, X., Andrés, N., Colucci, R.R., García-Hernández, C., Mora, C., Nofre, J., Palacios, D., Pérez-Alberti, A., Ribolini, A., Ruiz-Fernández, J., Sarıkaya, M.A., Serrano, E., Urdea, P., Valcárcel, M., Woodward, J.C., Yıldırım, C., 2018. Permafrost conditions in the Mediterranean region since the Last Glaciation. Earth-Science Rev. 185, 397–436. https://doi.org/10.1016/j.earscirev.2018.06.018

Osmaston, H., 2005. Estimates of glacier equilibrium line altitudes by the Area×Altitude, the Area×Altitude Balance Ratio and the Area×Altitude Balance Index methods and their validation. Quat. Int. 138–139, 22–31. https://doi.org/https://doi.org/10.1016/j.quaint.2005.02.004

Placer, L., 1998. Contribution to the macrotectonic subdivision of the border region between Southern Alps and External Dinarides = Prispevek k makrotektonski rajonizaciji mejnega ozemlja med Južnimi Alpami in Zunanjimi Dinaridi. Geologija 41, 223–255.

Plan, L., 2005. Factors controlling carbonate dissolution rates quantified in a field test in the Austrian alps. Geomorphology 68, 201–212.

https://doi.org/10.1016/J.GEOMORPH.2004.11.014

Pope, R.J., Hughes, P.D., Skourtsos, E., 2015. Glacial history of Mt Chelmos, Peloponnesus, Greece. Geol. Soc. London, Spec. Publ. 433. https://doi.org/10.1144/SP433.11

Pučnik, J., 1980. Velika knjiga o vremenu. Cankarjeva založba, Ljubljana.

Rea, B.R., 2009. Defining modern day Area-Altitude Balance Ratios (AABRs) and their use in glacier-climate reconstructions. Quat. Sci. Rev. 28, 237–248. https://doi.org/10.1016/J.QUASCIREV.2008.10.011

Reimer, P.J., Bard, E., Bayliss, A., Beck, J.W., Blackwell, P.G., Bronk Ramsey, C., Buck, C.E., Cheng, H., Edwards, R.L., Friedrich, M., Grootes, P.M., Guilderson, T.P., Haflidason, H., Hajdas, I., Hatté, C., Heaton, T.J., Hoffmann, D.L., Hogg, A.G., Hughen, K.A., Kaiser, K.F., Kromer, B., Manning, S.W., Niu, M., Reimer, R.W., Richards, D.A., Scott, E.M., Southon, J.R., Staff, R.A., Turney, C.S.M., van der Plicht, J., 2013. IntCal13 and Marine13 Radiocarbon Age Calibration Curves 0–50,000 Years cal BP. Radiocarbon 55, 1869–1887. https://doi.org/10.2458/azu_js_rc.55.16947

Reynolds, J.M., 1997. An Introduction to Applied and Environmental Geophysics. John Wiley & Sons Ltd, Chichester, UK.

Ribolini, A., Bini, M., Isola, I., Spagnolo, M., Zanchetta, G., Pellitero, R., Mechernich, S., Gromig, R., Dunai, T., Wagner, B., Milevski, I., 2018. An Oldest Dryas glacier expansion on Mount Pelister (Former Yugoslavian Republic of Macedonia) according to 10Be cosmogenic dating. J. Geol. Soc. London. 175, 100–110. https://doi.org/10.1144/jgs2017-038

Ribolini, A., Isola, I., Zanchetta, G., Bini, M., Sulpizio, R., 2011. Glacial features on the Galicica Mountains, Macedonia: Preliminary report. Geogr. Fis. e Din. Quat. 34, 247–255. https://doi.org/10.4461/GFDQ.2011.34.22

Rixhon, G., May, S.M., Engel, M., Mechernich, S., Schroeder-Ritzrau, A., Frank, N., Fohlmeister, J., Boulvain, F., Dunai, T., Brückner, H., 2018. Multiple dating approach (14C, 230Th/U and 36Cl) of tsunami-transported reef-top boulders on Bonaire (Leeward Antilles) – Current achievements and challenges. Mar. Geol. 396, 100–113. https://doi.org/https://doi.org/10.1016/j.margeo.2017.03.007

Ruszkiczay-Rüdiger, Z., Braucher, R., Novothny, Á., Csillag, G., Fodor, L., Molnár, G., Madarász, B., 2016a. Tectonic and climatic control on terrace formation: Coupling in situ produced 10Be depth profiles and luminescence approach, Danube River, Hungary, Central Europe. Quat. Sci. Rev. 131, 127–147. https://doi.org/10.1016/J.QUASCIREV.2015.10.041

Ruszkiczay-Rüdiger, Z., Kern, Z., Urdea, P., Braucher, R., Madarász, B., Schimmelpfennig, I., 2016b. Revised deglaciation history of the Pietrele–Stânişoara glacial complex, Retezat Mts, Southern Carpathians, Romania. Quat. Int. 415, 216–229. https://doi.org/10.1016/j.quaint.2015.10.085

Ryb, U., Matmon, A., Erel, Y., Haviv, I., Katz, A., Starinsky, A., Angert, A., Team, A., 2014. Controls on denudation rates in tectonically stable Mediterranean carbonate terrain. GSA Bull. 126, 553–568.

Schimmelpfennig, I., Benedetti, L., Finkel, R., Pik, R., Blard, P.-H., Bourlès, D., Burnard, P., Williams, A., 2009. Sources of in-situ 36Cl in basaltic rocks. Implications for calibration of production rates. Quat. Geochronol. 4, 441–461.

https://doi.org/https://doi.org/10.1016/j.quageo.2009.06.003

Schmidt, S., Hetzel, R., Kuhlmann, J., Mingorance, F., Ramos, V.A., 2011. A note of caution on the use of boulders for exposure dating of depositional surfaces. Earth Planet. Sci. Lett. 302, 60–70. https://doi.org/10.1016/j.epsl.2010.11.039

Šercelj, A., 1971. Postglacialni razvoj gorskih gozdov v severozahodni Jugoslaviji. Slovenska akademija znanosti in umetnosti, Ljubljana, pp. 30.

Sharma, P., Kubik, P.W., Fehn, U., Gove, H.E., Nishiizumi, K., Elmore, D., 1990. Development of 36Cl standards for AMS. Nucl. Instruments Methods Phys. Res. Sect. B Beam Interact. with Mater. Atoms 52, 410–415. https://doi.org/10.1016/0168-583X(90)90447-3

Siame, L., Bellier, O., Braucher, R., Sébrier, M., Cushing, M., Bourlès, D., Hamelin, B., Baroux, E., de Voogd, B., Raisbeck, G., Yiou, F., 2004. Local erosion rates versus active tectonics: cosmic ray exposure modelling in Provence (south-east France). Earth Planet. Sci. Lett. 220, 345–364. https://doi.org/10.1016/S0012-821X(04)00061-5

Šifrer, M., 1959. Obseg pleistocenske poledenitve na Notranjskem Snežniku. Geogr. Zb. 5, 27–83.

Šikić, D., Pleničar, M., Šparica, M., 1972. Osnovna geološka karta SFRJ. 1:100.000. List Ilirska Bistrica (Basic Geological Map of SFR Yugoslavia 1:100.000, Sheet Ilirska Bistrica). Zvezni geološki zavod, Beograd.

Sarıkaya, M., Çiner, A., 2017. Late Quaternary glaciations in the eastern Mediterranean, in: Hughes, P., Woodward, J. (Eds.), Quaternary Glaciation in the Mediterranean Mountains. Geological Society of London Special Publication 433, pp. 289–305. https://doi.org/10.1144/SP433.4

Silvester, P.P., Ferrari, R.L., 1990. Finite elements for electrical engineers (2nd. ed.). Cambridge Univ. Press.

Slaymaker, O., 2009. Proglacial, periglacial or paraglacial?, in: Knight, J., Harrison, S. (Eds.), Periglacial and Paraglacial Processes and Environments. The Geological Society of London, pp. 71–84.

Smart, C., 2004. Glacierized and glaciated karst, in: Gunn, J. (Ed.), Encyclopedia of Caves and Karst Science. Fitzroy Dearborn, New York, pp. 804–809.

Smart, P.L., 1986. Origin and development of glacio-karst closed depressions in the Picos de Europa, Spain. Zeitschrift für Geomorphol. 30, 423–443.

Stone, J.O., 2000. Air pressure and cosmogenic isotope production. J. Geophys. Res. Solid Earth 105, 23753–23759. https://doi.org/10.1029/2000JB900181

Stone, J.O., 2005. Terrestrial Chlorine-36 Production from Spallation of Iron, in: 10th AMS Conference. Berkeley.

Stone, J.O., Allan, G.L., Fifield, L.K., Cresswell, R.G., 1996. Cosmogenic chlorine-36 from calcium spallation. Geochim. Cosmochim. Acta 60, 679–692. https://doi.org/10.1016/0016-7037(95)00429-7

Styllas, M.N., Schimmelpfennig, I., Benedetti, L., Ghilardi, M., Aumaître, G., Bourlès, D., Keddadouche, K., 2018. Late-glacial and Holocene history of the northeast Mediterranean mountain glaciers - New insights from in situ-produced 36Cl-based cosmic ray exposure dating of paleo-glacier deposits on Mount Olympus, Greece. Quat. Sci. Rev. 193, 244–265. https://doi.org/https://doi.org/10.1016/j.quascirev.2018.06.020

Surina, B., Wraber, T., 2005. Phytosociology and ecology of Carex mucronata on the Mt. Snežnik (SW Slovenia, Liburnian Karst). Wulfenia 12, 97–112.

Thomas, F., Godard, V., Bellier, O., Benedetti, L., Ollivier, V., Rizza, M., Guillou, V., Hollender, F., Aumaître, G., Bourlès, D.L., Keddadouche, K., 2018. Limited influence of climatic gradients on the denudation of a Mediterranean carbonate landscape. Geomorphology 316, 44–58. https://doi.org/10.1016/J.GEOMORPH.2018.04.014

Veress, M., 2017. Solution DOLINE development on GLACIOKARST in alpine and Dinaric areas. Earth-Science Rev. 173, 31–48. https://doi.org/10.1016/J.EARSCIREV.2017.08.006

Vrabec, M., Fodor, L., 2006. Late Cenozoic tectonics of Slovenia: structural styles at the Northeastern corner of the Adriatic microplate, in: Pinter, N., Grenerczy, G., Weber, J., Stein, S., Medak, D. (Eds.), The Adria Microplate: GPS Geodesy, Tectonics and Hazards, NATO Science Series. Springer, Dordrecht, pp. 151–168.

Woodward, J., Macklin, M., Hughes, P., Adamson, K.R., Lewin, J., 2014. The paraglacial concept revisited : the record from the Mediterranean mountains of Southern Europe, in: Geophysical Research Abstracts, Vol. 16, EGU2014-5517. p. 5517.

Zaninović, K., Gajić-Čapka, M., Perčec Tadić, M., Vučetić, M., Milković, J., Bajić, A., Cindrić, K., Cvitan, L., Katušin, Z., Kaučić, D., Likso, T., Lončar, Ž., Mihajlović, D., Pandžić, K., Patarčić, M., Srnec, L., Vučetić, V., 2008. Klimatski atlas Hrvatske / Climate atlas of Croatia 1961-1990., 1971-2000. Meteorological and Hydrological Service of Croatia, Zagreb.

Žebre, M., 2015. Pleistocenska poledenitev obalnega dela Dinarskega gorstva (Pleistocene Glaciation of the Coastal Dinaric Mountains) (PhD thesis). Faculty of Arts, University of Ljubljana, Ljubljana, pp. 197.

Žebre, M., Stepišnik, U., 2014. Reconstruction of Late Pleistocene glaciers on Mount Lovćen, Montenegro. Quat. Int. 353, 225–235. https://doi.org/10.1016/j.quaint.2014.05.006

Žebre, M., Stepišnik, U., 2015. Glaciokarst landforms and processes of the southern Dinaric Alps. Earth Surf. Process. Landforms 40, 1493–1505. https://doi.org/10.1002/esp.3731

Žebre, M., Stepišnik, U., 2016. Glaciokarst geomorphology of the Northern Dinaric Alps: Snežnik (Slovenia) and Gorski Kotar (Croatia). J. Maps 12, 873–881. https://doi.org/10.1080/17445647.2015.1095133

Žebre, M., Stepišnik, U., Colucci, R.R., Forte, E., Monegato, G., 2016. Evolution of a karst polje influenced by glaciation: The Gomance piedmont polje (northern Dinaric Alps). Geomorphology 257, 143–154. https://doi.org/10.1016/j.geomorph.2016.01.005

Žebre, M., Stepišnik, U., Kodelja, B., 2013. Traces of Pleistocene glaciation on Trnovski gozd | Sledovi pleistocenske Poledenitve na Trnovskem gozdu. Dela 39, 157–170. https://doi.org/10.43121/dela.39.9.157-170

Supplementary material

Element	CRN PD-02/ 25-30	CRN PD-02/ 75-80	CRN PD-02/ 105-110	Average
Fusion inductively coupled plasma (FUS-ICP AES)				
SiO_2	4,73%	0,71%	0,75%	2,06%
Al_2O_3	0,31%	0,13%	0,19%	0,21%
Fe_2O_3	0,21%	0,10%	0,12%	0,14%
MnO	0,007%	0,004%	0,003%	0,005%
MgO	1,70%	1,24%	1,39%	1,44%
CaO	51,3%	53,8%	54,6%	53,2%
Na_2O	0,0007	0,03%	0,07%	0,06%
K_2O	0,06%	0,02%	0,04%	0,04%
TiO_2	0,027%	0,007%	0,004%	0,013%
P_2O_5	< 0.01 %	0,01%	0,01%	0,01%
CO_2 (LOI)	40,6%	42,7%	42,4%	41,9%
Total	99,0%	98,7%	99,51%	99,07%
Gravimetric				
H_2O	0,3%	0,3%	0,2%	0,27%
Fusion mass spectrometry (FUS-ICP MS)				
Rb	< 2 µg/g	< 2 µg/g	< 2 µg/g	0 µg/g
Sm	0.5 µg/g	< 0.1 µg/g	< 0.1 µg/g	0.2 µg/g
Gd	0.6 µg/g	0.1 µg/g	< 0.1 µg/g	0.2 µg/g
Th	0.2 µg/g	< 0.1 µg/g	< 0.1 µg/g	0.1 µg/g
U	1.5 µg/g	2.2 µg/g	3.1 µg/g	2.3 µg/g
Fusion inductively coupled plasma (FUS-ICP AES)				
Ba	12 µg/g	6 µg/g	6 µg/g	
Sr	190 µg/g	254 µg/g	227 µg/g	224 µg/g
Zr	10 µg/g	3 µg/g	4 µg/g	5.67 µg/g
Total digestion inductively coupled plasma (TD-ICP)				
Li	1 µg/g	< 1 µg/g	< 1 µg/g	0.3 µg/g
Prompt gamma neutron activation analysis (PGNAA)				
B	< 0.5 µg/g	< 0.5 µg/g	7.3 µg/g	2.5 µg/g
Accelerator Mass Spectroscopy (AMS; Table S1)				
Cl	47.3 µg/g	48.5 µg/g	49.7 µg/g	49.6 µg/g

Table S1. Relevant chemical composition of untreated samples measured at Activation laboratories (Canada) and by AMS (accelerator mass spectrometry; measurements in this study). Values below detection limit are marked with "<". LOI:

loss on ignition. The average composition of the three samples was used for the depth profile modelling.

Sample ID [a]	Sample weight	Spike [b] weight	$^{36}Cl/^{35}Cl$ [c] (-)	± $^{36}Cl/^{35}Cl$ (-)	$^{36}Cl/^{37}Cl$ [c] (-)	± $^{36}Cl/^{37}Cl$ (-)	$^{35}Cl/^{37}Cl$ [c] (-)	± $^{35}Cl/^{37}Cl$ (-)	^{36}Cl conc. (atoms g^{-1})	±^{36}Cl conc. (atoms g^{-1})	±^{36}Cl conc. (%)	Cl_{nat} AMS (µg/g)	±Cl_{nat} AMS (µg/g)	blank correction (%)	^{36}Cl total prod. rate [d] (atoms/g/yr)	^{36}Cl prod. by neutrons [d] (atoms/g/yr)	^{36}Cl prod. thermal neutrons [d] (atoms/g/yr)	^{36}Cl prod.by by muons [d] (atoms/g/yr)
CRN PD-02/25-30	20,1379	1,4848	2,81E-13	1,18E-14	1,98E-12	8,29E-14	7,05	0,04	5,11E+05	2,26E+04	4,4%	47,3	1,9	0,41%	41,23	26,09	9,33	4,83
CRN PD-02/75-80	20,4658	1,4892	1,73E-13	8,17E-15	1,20E-12	5,67E-14	6,94	0,04	3,14E+05	1,56E+04	5,0%	48,5	2,0	0,66%	24,37	13,15	6,17	4,51
CRN PD-02/ 105-110	19,7269	1,4859	1,39E-13	5,71E-15	9,71E-13	3,98E-14	6,97	0,04	2,61E+05	1,14E+04	4,4%	49,7	2,0	0,82%	17,76	8,71	4,34	4,33
CRN PD-02/ 215-220	29,6144	1,4832	2,02E-13	7,29E-15	1,19E-12	4,31E-14	5,91	0,04	2,95E+05	1,21E+04	4,1%	49,6	2,2	0,48%	7,15	1,93	1,36	3,71
Blank B17/05	-	1,3861	1,85E-15	4,51E-16	3,48E-14	8,47E-15	18,78	0,11	-	-	-	-	-	-	-	-	-	-
CoCal-N_UEdin-CologneAMS-1	8,4195	1,1907	1,55E-12	4,18E-14	2,86E-11	7,73E-13	18,48	0,31	3,62E+06	9,95E+04	2,7%	1,3	0,9	0,35%	-	-	-	-
CoCal-N_UEdin-CologneAMS-2	8,6312	1,1891	1,64E-12	4,45E-14	3,04E-11	8,25E-13	18,56	0,31	3,74E+06	1,03E+05	2,8%	1,1	0,8	0,33%	-	-	-	-
CoCal-N_UEdin-CologneAMS-3	8,7859	1,1880	1,65E-12	4,76E-14	3,08E-11	8,86E-13	18,63	0,31	3,69E+06	1,08E+05	2,9%	1,0	0,8	0,33%	-	-	-	-
CoCal-N_UEdin-CologneAMS-4	8,3094	1,1940	1,56E-12	4,37E-14	2,89E-11	8,09E-13	18,51	0,31	3,71E+06	1,05E+05	2,8%	1,3	0,9	0,34%	-	-	-	-
CoCal-N_UEdin-CologneAMS-5	5,8187	1,1901	1,09E-12	3,75E-14	2,05E-11	7,05E-13	18,98	0,32	3,64E+06	1,28E+05	3,5%	0,5	1,2	0,50%	-	-	-	-
CoCal-N_UEdin-CologneAMS-6	5,6722	0,8387	1,53E-12	4,47E-14	2,82E-11	8,24E-13	18,46	0,31	3,74E+06	1,11E+05	3,0%	0,8	1,1	0,50%	-	-	-	-
CoCal-N_UEdin-CologneAMS-7	5,7713	1,1923	1,09E-12	3,35E-14	2,02E-11	6,22E-13	18,61	0,31	3,71E+06	1,16E+05	3,1%	1,6	1,3	0,50%	-	-	-	-
CoCal-N_UEdin-CologneAMS-8	5,5543	1,1874	1,03E-12	2,95E-14	1,90E-11	5,47E-13	18,53	0,31	3,62E+06	1,06E+05	2,9%	1,9	1,3	0,53%	-	-	-	-
CoCal-N_UEdin-CologneAMS-9	11,2870	1,1896	2,13E-12	5,96E-14	3,97E-11	1,11E-12	18,67	0,31	3,71E+06	1,05E+05	2,8%	0,7	0,6	0,25%	-	-	-	-
Blank-CoCal-Uedin	-	1,1863	5,49E-15	1,53E-15	1,04E-13	2,90E-14	19,16	0,32	-	-	-	-	-	-	-	-	-	-

[a] The CoCal-N intercomparison material yields an initial consensus value of (3.74 ± 0.10) x 10^6 at ^{36}Cl/g and 0.73 ± 0.18 µg/g of natural chlorine (Mechernich et al., 2019).

[b] Chlorine mass of $^{35}Cl/^{37}Cl$ spike added to the sample prior to dissolution. Spike concentration: mg Cl/g solution = 5.4569, $^{35}Cl/^{37}Cl$ = 19.960.

[c] The AMS machines were calibrated and normalized to three different concentrated standards (^{36}Cl/Cl: 5.000×10^{-13}, 1.600×10^{-12}, and 1.000×10^{-11}) from the NIST SRM 4943 material (Sharma et al., 1990).

[d] All given production rates account for the case of no erosion.

Table S2. ^{36}Cl sample preparation details and resulting Cl AMS ratios, ^{36}Cl and natural chlorine concentrations, and the sample-specific ^{36}Cl production rates. All errors are given as 1σ uncertainties.